The clustering of galaxies in the SDSS-III Baryon Oscillation Spectroscopic Survey: measuring growth rate and geometry with anisotropic clustering

Journal Item

Version: Version of Record

Link(s) to article on publisher's website:
http://dx.doi.org/doi:10.1093/mnras/stu197

Monthly Notices
of the
ROYAL ASTRONOMICAL SOCIETY

MNRAS **439,** 3504–3519 (2014)
Advance Access publication 2014 February 27

doi:10.1093/mnras/stu197

The clustering of galaxies in the SDSS-III Baryon Oscillation Spectroscopic Survey: measuring growth rate and geometry with anisotropic clustering

Lado Samushia,[1,2★] Beth A. Reid,[3,4†] Martin White,[3,4] Will J. Percival,[1] Antonio J. Cuesta,[5,6] Gong-Bo Zhao,[1,7] Ashley J. Ross,[1] Marc Manera,[8,1] Éric Aubourg,[9] Florian Beutler,[3] Jon Brinkmann,[10] Joel R. Brownstein,[11] Kyle S. Dawson,[11] Daniel J. Eisenstein,[12] Shirley Ho,[13] Klaus Honscheid,[14] Claudia Maraston,[1] Francesco Montesano,[15] Robert C. Nichol,[1] Natalie A. Roe,[3] Nicholas P. Ross,[3,16] Ariel G. Sánchez,[15] David J. Schlegel,[3] Donald P. Schneider,[17,18] Alina Streblyanska,[19,20] Daniel Thomas,[1] Jeremy L. Tinker,[21] David A. Wake,[22,23] Benjamin A. Weaver[21] and Idit Zehavi[24]

[1] *Institute of Cosmology and Gravitation, University of Portsmouth, Dennis Sciama Building, Portsmouth P01 3FX, UK*
[2] *National Abastumani Astrophysical Observatory, Ilia State University, 2A Kazbegi Ave., GE-1060 Tbilisi, Georgia*
[3] *Lawrence Berkeley National Laboratory, 1 Cyclotron Road, Berkeley, CA 94720, USA*
[4] *Departments of Physics and Astronomy, University of California, Berkeley, CA 94720, USA*
[5] *Department of Physics, Yale University, 260 Whitney Ave, New Haven, CT 06520, USA*
[6] *Institut de Ciències del Cosmos, Universitat de Barcelona, IEEC-UB, Martí Franquès 1, E-08028 Barcelona, Spain*
[7] *National Astronomy Observatories, Chinese Academy of Science, Beijing 100012, P.R. China*
[8] *University College London, Gower Street, London WC1E 6BT, UK*
[9] *APC, Univ Paris Diderot, CNRS/IN2P3, CEA/Irfu, Obs de Paris, Sorbonne Paris Cit, F-75205, France*
[10] *Apache Point Observatory, 2001 Apache Point Road, Sunspot, NM 88349, USA*
[11] *Department of Physics and Astronomy, University of Utah, 115 S 1400 E, Salt Lake City, UT 84112, USA*
[12] *Harvard–Smithsonian Center for Astrophysics 60 Garden St Cambridge, MA 02138, USA*
[13] *Department of Physics, Carnegie Mellon University, 5000 Forbes Avenue, Pittsburgh, PA 15213, USA*
[14] *Department of Physics and Center for Cosmology and Astro-Particle Physics, Ohio State University, Columbus, OH 43210, USA*
[15] *Max-Planck-Institut für Extraterrestrische Physik, Giessenbachstrasse, D-85748 Garching, Germany*
[16] *Department of Physics, Drexel University, 3141 Chestnut Street, Philadelphia, PA 19104, USA*
[17] *Department of Astronomy and Astrophysics, The Pennsylvania State University, University Park, PA 16802, USA*
[18] *Institute for Gravitation and the Cosmos, The Pennsylvania State University, University Park, PA 16802, USA*
[19] *Instituto de Astrofísica de Canarias (IAC), E-38200 La Laguna, Tenerife, Spain*
[20] *Universidad de La Laguna (ULL), Dept. Astrofísica, E-38206 La Laguna, Tenerife, Spain*
[21] *Center for Cosmology and Particle Physics, New York University, New York, NY 10003, USA*
[22] *Department of Astronomy, University of Wisconsin-Madison, 475 N. Charter Street, Madison, WI 53706, USA*
[23] *Department of Physical Sciences, The Open University, Milton Keynes MK7 6AA, UK*
[24] *Department of Astronomy, Case Western Reserve University, Cleveland, OH 44106, USA*

Accepted 2014 January 27. Received 2014 January 27; in original form 2013 December 18

ABSTRACT

We use the observed anisotropic clustering of galaxies in the Baryon Oscillation Spectroscopic Survey Data Release 11 CMASS sample to measure the linear growth rate of structure, the Hubble expansion rate and the comoving distance scale. Our sample covers 8498 deg^2 and encloses an effective volume of 6 Gpc^3 at an effective redshift of $\bar{z} = 0.57$. We find $f\sigma_8 = 0.441 \pm 0.044$, $H = 93.1 \pm 3.0\,\mathrm{km\,s^{-1}\,Mpc^{-1}}$ and $D_\mathrm{A} = 1380 \pm 23\,\mathrm{Mpc}$ when fitting the growth and expansion rate simultaneously. When we fix the background expansion to the

★ E-mail: lado.samushia@port.ac.uk
† Hubble Fellow.

one predicted by spatially flat Λ cold dark matter (ΛCDM) model in agreement with recent *Planck* results, we find $f\sigma_8 = 0.447 \pm 0.028$ (6 per cent accuracy). While our measurements are generally consistent with the predictions of ΛCDM and general relativity, they mildly favour models in which the strength of gravitational interactions is weaker than what is predicted by general relativity. Combining our measurements with recent cosmic microwave background data results in tight constraints on basic cosmological parameters and deviations from the standard cosmological model. Separately varying these parameters, we find $w = -0.983 \pm 0.075$ (8 per cent accuracy) and $\gamma = 0.69 \pm 0.11$ (16 per cent accuracy) for the effective equation of state of dark energy and the growth rate index, respectively. Both constraints are in good agreement with the standard model values of $w = -1$ and $\gamma = 0.554$.

Key words: gravitation – cosmological parameters – dark energy – dark matter – distance scale – large-scale structure of Universe.

1 INTRODUCTION

Galaxies map the distribution of the underlying dark matter field and provide invaluable information about both the nature of dark energy (DE) and properties of gravity (see e.g. Weinberg et al. 2013). The shape of the two-point correlation function of the observed galaxy field, or of its Fourier-transform – the power-spectrum, contains features such as baryon acoustic oscillations (BAO) and the turnover marking the transition between radiation-dominated and matter-dominated evolutionary phases (Eisenstein & Hu 1998; Meiksin, White & Peacock 1999). These features can be used to place tight constraints on relative abundances of different energy-density components of the Universe (radiation ρ_γ, dark matter $\rho_{\rm dm}$, baryonic matter $\rho_{\rm b}$ and DE $\rho_{\rm DE}$). Presently, these ratios are measured to much higher accuracy in the cosmic microwave background (CMB; Planck Collaboration 2013). Therefore, for most cosmological models these features provide most information when used as a standard ruler.

If the Universe is statistically isotropic and homogeneous on large scales, the correlation function and power spectrum should likewise be rotationally invariant. The observed two-point statistics instead exhibit a strong anisotropy with respect to the line-of sight (LOS) direction. Two effects are responsible for this apparent anisotropy: the redshift-space distortions (RSD; Kaiser 1987) and the Alcock–Paczynski effect (AP; Alcock & Paczynski 1979).

The RSD arise in maps made from galaxies if distances are determined from measured redshifts assuming that they are only caused by the Hubble flow. Because of gravitational growth, the galaxies tend to infall towards high-density regions and flow away from low-density regions, such that the clustering is enhanced in the LOS direction compared to the perpendicular direction. The observed redshifts thus have a component aligned with these flows. On large scales where gravitational growth is linear, measuring the relative clustering in both LOS and transverse directions leads to a measurement of the logarithmic growth rate of structure

$$f(a)\sigma_8(a) = \sigma_8(a=1)\frac{{\rm d}G(a)}{{\rm d}\ln a}, \tag{1}$$

where a is a scalefactor, $\sigma_8(a)$ is a measure of the amplitude of the matter power spectrum and $G(a)$ is the linear growth function normalized such that $G(a=1)=1$ (see Hamilton 1998 for a review of RSD).

The magnitude of the large-scale velocity field traced by galaxies depends on the nature of gravitational interactions, and measured values of $f\sigma_8$ can be used to constrain models of gravity (see e.g. Guzzo et al. 2008). Galaxy clustering data measures the growth at low redshifts. Combining this information with the accurate estimates of the amplitude of matter perturbations at $z \sim 1000$ provided by CMB allows for extremely strong constraints for deviations from the predictions of general relativity (GR) since even small changes in the growth of structure accumulate to a large offset over cosmic time (for recent GR constraints see e.g. Zhao et al. 2012; Rapetti et al. 2013; Samushia et al. 2013; Sanchez et al. 2013a; Simpson et al. 2013).

Anisotropies are also observed due to the AP effect, which stems from the fact that we need to convert observed angular positions and redshifts of galaxies to physical coordinates in order to measure clustering statistics. If the fiducial cosmology used for this mapping is different from the true cosmology, this will induce anisotropies in the measured clustering pattern even in the absence of RSD. Angular distortions are sensitive to the offset in the angular distance $D_{\rm A}(z)$ and distortions in the LOS direction depend on the offset in $H(z)$. Measuring the AP effect provides accurate estimates of the angular distance and Hubble parameter and can be used to constrain properties of DE (see e.g. Eisenstein, Seo & White 2007). Measurements of both angular and radial projected scales are usually reported in terms of the volume-averaged distance

$$D_{\rm V} = \left[(1+z)^2 cz\frac{D_{\rm A}^2}{H}\right]^{1/3}, \tag{2}$$

and the AP parameter

$$F = \frac{1+z}{c} D_{\rm A} H. \tag{3}$$

In the absence of RSD, the measured correlation function monopole would be sensitive mostly to isotropic scale dilation through $D_{\rm V}$ and the quadrupole to anisotropic scale dilation through F. Most of the information on $D_{\rm V}$ usually comes from the most pronounced feature in the correlation function – the position of the BAO peak in the monopole. It is therefore convenient to report results in terms of $D_{\rm V}/r_{\rm d}$, where $r_{\rm d}$ is the sound horizon at the drag epoch which sets the BAO scale (for a review of BAO and AP see e.g. Bassett & Hlozek 2010).

The RSD and AP are partially degenerate but have a different scale dependence which makes their simultaneous measurement possible (Ballinger, Peacock & Heavens 1996). Specifying cosmological models of background expansion or gravity helps to further break this degeneracy (e.g. Samushia et al. 2011). Measuring correlation function in different fiducial cosmological models and fitting the RSD signal in each can help to reduce the degeneracy as well (Marulli et al. 2012).

The RSD signal within the correlation function is difficult to model because of the significant contribution from non-linear effects and higher order contributions from galaxy bias. A number of recent studies have shown that many current RSD models result in biased estimates of the growth rate (see e.g. Bianchi et al. 2012; de la Torre & Guzzo 2012; Gil-Marin et al. 2012). In our work, we use the 'streaming model'-based approach developed in Reid & White (2011) that has been demonstrated to fit the monopole and quadrupole of the galaxy correlation function with better than per cent level precision to scales above $25\,h^{-1}$ Mpc, for galaxies with bias of $b \simeq 2$.[1]

Many distance-scale and RSD measurements have previously been made using spectroscopic survey data. Recent highlights include the BAO measurements from the 6dF Galaxy Redshift Survey (6dFGRS; Beutler et al. 2011), Sloan Digital Sky Survey II (SDSS-II; Padmanabhan et al. 2012), SDSS-III Baryon Oscillation Spectroscopic Survey (BOSS) Data Release 9 sample (DR9; Anderson et al. 2012), WiggleZ survey (Blake et al. 2011b) and SDSS-III BOSS DR10 and DR11 samples (Anderson et al. 2013). The RSD signal has been measured in the 6dFGRS (Beutler et al. 2012), the SDSS-II survey (Samushia, Percival & Raccanelli 2012), the SDSS-III BOSS DR9 data (Reid et al. 2012) and VIMOS Public Extragalactic Redshift Survey (VIPERS; de la Torre et al. 2013). Simultaneous fits to RSD and AP parameters have been performed for the WiggleZ survey (Blake et al. 2012), SDSS-II data (Chuang & Wang 2013) and SDSS-III BOSS DR9 data (Reid et al. 2012).

The analysis presented in this paper builds upon that of Reid et al. (2012), who measured the RSD and AP simultaneously in the BOSS CMASS DR9 sample, achieving a 15 per cent measurement of growth, 2.8 per cent measurement of angular diameter distance and 4.6 per cent measurement of the expansion rate at $z = 0.57$. Using these estimates Samushia et al. (2013) derived strong constraints on modified theories of gravity (MG) and DE model parameters. In this paper, we perform a similar analysis on the CMASS DR11 sample, which covers roughly three times the volume of DR9.

This paper is organized as follows. In Section 2, we describe the data used in the analysis. Section 3 explains how the two-dimensional correlation function is estimated from the data. Section 4 shows how we derive the estimates of the covariance matrix for our measurements. In Section 5, we describe the theoretical model used to fit the data. Section 6 presents and discusses our main results – the estimates of growth rate, distance–redshift relationship and the expansion rate from the measurements. Section 7 uses these estimates to constrain parameters in the Λ cold dark matter (ΛCDM) model assuming GR (ΛCDM-GR) and possible deviations from this standard model. We conclude and discuss our results in Section 8.

Our measurements require the adoption of a cosmological model in order to convert angles and redshifts into comoving distances. As in Anderson et al. (2013), we adopt a spatially flat ΛCDM cosmology with $\Omega_{\rm m} = 0.274$ and $h = 0.7$ for this purpose. For ease of comparison across analyses, we follow Anderson et al. (2013) and also report our distance constraints relative to a model with $\Omega_{\rm m} = 0.274$, $h = 0.7$ and $\Omega_{\rm b}h^2 = 0.0224$, for which the BAO scale $r_{\rm d} = 149.31$ Mpc.

[1] For alternative approaches to modelling the non-linear effects in RSD see e.g. Taruya, Nishimichi & Saito (2010), Okamura, Taruya & Matsubara (2011), Elia et al. (2011), Crocce, Scoccimarro & Bernardeau (2012) and Vlah et al. (2012). For updates to the streaming model see Wang, Reid & White (2014).

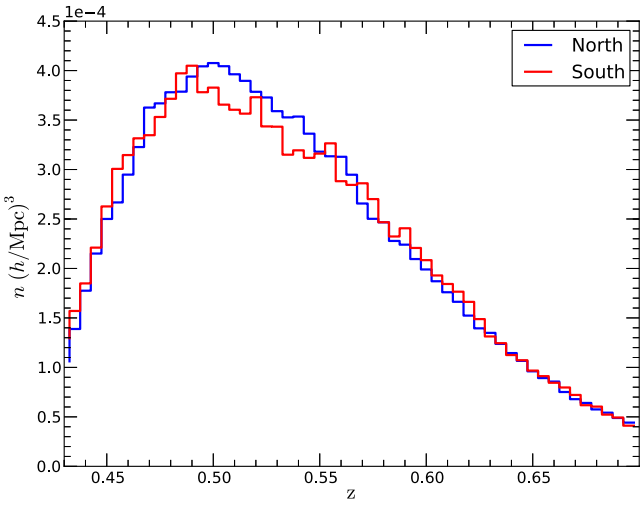

Figure 1. The number density of CMASS DR11 galaxies in redshift bins of $\Delta z = 0.01$ in northern and southern Galactic hemispheres, computed assuming our fiducial cosmology.

2 THE DATA

The SDSS-III project (Eisenstein et al. 2011) uses a dedicated 2.5 m Sloan telescope (Gunn et al. 2013) to perform spectroscopic follow-up of targets selected from images made using a now-retired drift-scanning mosaic CCD camera (Gunn et al. 2006) that imaged the sky in five photometric bands (Fukugita et al. 1996) to a limiting magnitude of $r \simeq 22.5$. The BOSS (Dawson et al. 2013) is the part of SDSS-III that will measure spectra for 1.5 million galaxies and 160.000 quasars over a quarter of the sky.

We use the DR11 CMASS sample of galaxies (Bolton et al. 2012; Anderson et al. 2013; Smee et al. 2013). This lies in the redshift range of $0.43 < z < 0.70$ and consists of 690 826 galaxies covering 8498 square degrees (effective volume of $6\,{\rm Gpc}^3$). Most galaxies in the sample belong to the red sequence. About 25 per cent of them, however, would be classified as 'blue' according to traditional SDSS rest-frame colour cuts (see e.g. Strateva et al. 2001). Ross et al. (2014) showed that there is no detectable colour dependence of distance-scale and growth-rate measurements in DR10 sample.

Fig. 1 shows the redshift distribution of galaxies in our sample. The number density is of the order of 10^{-4} peaking at $\bar{n} \simeq 4 \times 10^{-4}\,h^3\,{\rm Mpc}^{-3}$.

3 THE MEASUREMENTS

We measure the correlation function of galaxies in the CMASS sample defined as the ensemble average of the product of overdensities in the galaxy field separated by a certain distance $\boldsymbol{r}$

$$\xi(\boldsymbol{r}) \equiv \langle \delta_{\rm g}(\boldsymbol{r}')\delta_{\rm g}(\boldsymbol{r}'+\boldsymbol{r})\rangle. \quad (4)$$

The overdensity as a function of $\boldsymbol{r}$ is given by

$$\delta_{\rm g}(\boldsymbol{r}) = \frac{n_{\rm g}(\boldsymbol{r}) - \bar{n}_{\rm g}(\boldsymbol{r})}{\bar{n}_{\rm g}(\boldsymbol{r})}, \quad (5)$$

where $\bar{n}_{\rm g}(\boldsymbol{r})$ is the expected average density of galaxies at a position $\boldsymbol{r}$, and $n_{\rm g}(\boldsymbol{r})$ is an observed number density.

We estimate the correlation function using the Landy–Szalay minimum-variance estimator (Landy & Szalay 1993)

$$\hat{\xi}(\Delta\boldsymbol{r}_i) = \frac{DD(\Delta\boldsymbol{r}_i) - 2DR(\Delta\boldsymbol{r}_i) + RR(\Delta\boldsymbol{r}_i)}{RR(\Delta\boldsymbol{r}_i)}, \quad (6)$$

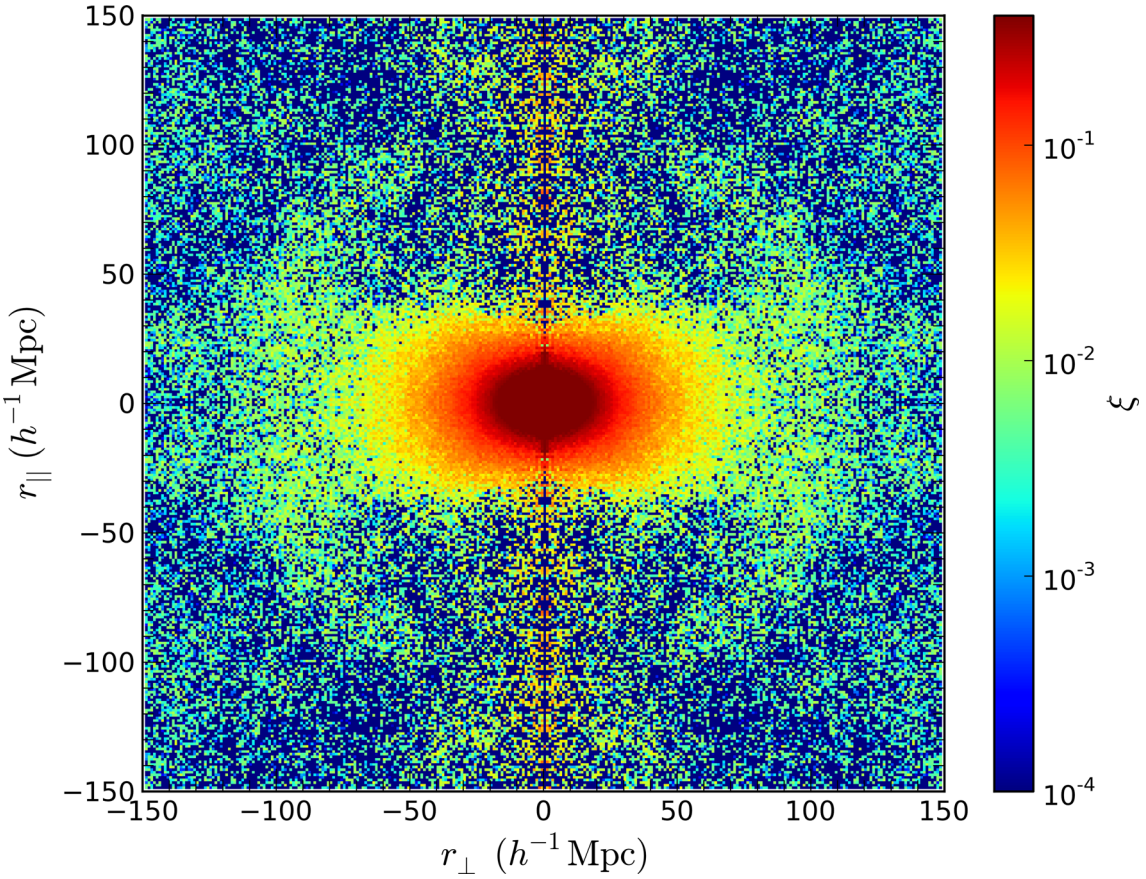

Figure 2. The two-dimensional correlation function of DR11 sample measured in bins of $1\,h^{-1} \times 1\,h^{-1}$ Mpc^2. We use first two Legendre multipoles of the correlation function in our study rather than the two-dimensional correlation function displayed here.

where $DD(\Delta \boldsymbol{r}_i)$ is the weighted number of galaxy pairs whose separation falls within the $\Delta \boldsymbol{r}_i$ bin, $RR(\Delta \boldsymbol{r}_i)$ is number of similar pairs in the random catalogue and $DR(\Delta \boldsymbol{r}_i)$ is the number of cross-pairs between the galaxies and the objects in the random catalogue.

Fig. 2 shows the two-dimensional correlation function of DR11 sample measured in bins of $1\,h^{-1} \times 1\,h^{-1}$ Mpc^2. Both the 'BAO ridge' (a ring of local maxima at approximately $100\,h^{-1}$ Mpc) and the RSD signal (LOS 'squashing' of the correlation function) are detectable by eye.

The random catalogue is constructed by populating the volume covered by galaxies with random points with zero correlation. We use a random catalogue that has 50 times the density of galaxies to eliminate extra uncertainty associated with the shot noise in the random catalogue.

We weight each galaxy in the catalogue with three independent weights. First is the Feldman–Kaiser–Peacock (FKP; Feldman, Kaiser & Peacock 1994) weight $w_{\rm FKP} = 1/[1 + \bar{n}(z)20\,000]$. This approach downweights galaxies in high-density regions, achieving a balance between cosmic variance and shot-noise errors. The second weight $w_{\rm sys} = w_{\rm star} w_{\rm see}$ accounts for the systematic effects associated with both the varying stellar density ($w_{\rm star}$; Ross et al. 2012) and seeing variations in the imaging catalogue used for targeting ($w_{\rm see}$; Anderson et al. 2013). The third weight corrects for the missed galaxies due to fibre collisions and redshift failures using the algorithm described in Anderson et al. (2012). The former is caused by the finite size of fibres that makes simultaneous measurement of spectra of two galaxies with small angular separation impossible. To correct for both of these effects, we upweight each galaxy by the number of its lost neighbours and the resulting weight is $(w_{\rm cp} + w_{\rm zf} - 1)$. Since these effects are statistically independent, the total weight is a product of three $w_{\rm tot} = w_{\rm FKP} w_{\rm sys}(w_{\rm cp} + w_{\rm zf} - 1)$. The weight of the pair is the product of individual weights for two galaxies. Since the stellar and close-pair effects are absent in the random catalogue, we apply only the FKP weight to them.

The observed correlation function is a function of two variables: we use r, the distance between galaxies, and μ, the cosine of the angle between their connecting vector and the LOS. The optimal choice of binning for the correlation function measurements depends on two competing effects. Using small bin size retains more information, but since we estimate covariance matrices by computing a scatter of finite number of mock catalogues (see Section 4), using more bins deteriorates the precision at which the elements of the covariance matrices can be estimated. Empirical tests performed on the mock catalogues suggest that the RSD signal is more or less insensitive to the binning choice, while the BAO measurements are optimal at $\sim 8\,h^{-1}$ Mpc (for details see Percival et al. 2013). We bin r in 16 bins of $8\,h^{-1}$ Mpc in size in the range of $24\,h^{-1} < r < 152\,h^{-1}$ Mpc and μ in 200 bins in $0 < \mu < 1$, and estimate the correlation function on this two-dimensional grid. The information in the correlation function below $24\,\mathrm{Mpc}\,h^{-1}$ is strongly contaminated by non-linear effects, and the scales above $152\,\mathrm{Mpc}\,h^{-1}$ have low signal-to-noise ratio and contribute little information.

We compress the information in the two-dimensional correlation function by computing the Legendre multipoles with respect to μ

by approximating the integral with a discrete sum:

$$\hat{\xi}_\ell(r_i) = \frac{2\ell+1}{2}\int_{-1}^{1} \mathrm{d}\mu\, \hat{\xi}(r_i,\mu)L_\ell(\mu) \tag{7}$$

$$\approx \frac{2\ell+1}{2}\sum_k \Delta\mu_k\, \hat{\xi}(r_i,\mu_k)L_\ell(\mu_k), \tag{8}$$

where $L_\ell(\mu)$ is the Legendre polynomial of the order of ℓ.

In the subsequent analysis, we only use the monopole ($\ell = 0$) and the quadrupole ($\ell = 2$) moments. The higher order moments contain significantly less information and are more difficult to model. (For the contribution of the higher order moments, see e.g. Taruya, Saito & Nishimichi 2011; Kazin, Sanchez & Blanton 2012).

The RSD signal in the measured correlation function varies within the sample due to redshift evolution [via the redshift dependence of $f(z)\sigma_8(z)$ and $b(z)\sigma_8(z)$] . If we keep track of the redshift of individual galaxy pairs in equation (6), we effectively measure

$$\hat{\xi} = \frac{\sum \xi(z_i)w_i^2}{\sum w_i^2}, \tag{9}$$

where summation is over individual galaxy pairs contributing to *DD* counts, $\xi(z_i)$ is the correlation function at mean redshift of that galaxy pair and w_i^2 is the product of the weights of individual galaxies in the ith pair. Thus, our measurement is actually a weighted redshift-averaged correlation function. The evolving correlation function can be expanded into Taylor series in redshift around some value of $\bar{z}$:

$$\xi(z) = \xi(\bar{z}) + \left.\frac{\mathrm{d}\xi}{\mathrm{d}z}\right|_{z=\bar{z}} (\bar{z}-z) + \mathcal{O}\left[(\bar{z}-z)^2\right]. \tag{10}$$

Keeping only the first-order term, we find

$$\xi = \xi(\bar{z}) + \left.\frac{\mathrm{d}\xi}{\mathrm{d}z}\right|_{z=\bar{z}} \frac{\sum(\bar{z}-z_i)w_i^2}{\sum w_i^2}, \tag{11}$$

and the second term disappears if we define

$$\bar{z} = \frac{\sum z_i w_i^2}{\sum w_i^2}. \tag{12}$$

If the derivatives of the correlation function of second order and higher are small, the redshift-averaged correlation function is equal to the correlation function at an 'effective' redshift given by equation (12).

The 'effective' redshift defined in equation (12) is a function of scale. We adopt $\bar{z} = 0.57$, a value which is close to the $\bar{z}$ computed from the catalogue to better than 1 per cent precision for all scales in the range $24\,h^{-1} < r < 152\,h^{-1}$ Mpc. We checked that in our fiducial ΛCDM cosmology the contribution from the higher order terms in equation (11) are indeed small for the expected theoretical variations in $f\sigma_8$ within the redshift range. We will therefore interpret our estimates as measurements of the correlation function at this effective redshift.

Fig. 3 shows the measured monopole and quadrupole of the CMASS galaxies along with 1σ error bars (see Section 4 for details of the error estimation). We will use these measurements in our analysis rather than the two-dimensional correlation function presented in Fig. 2.

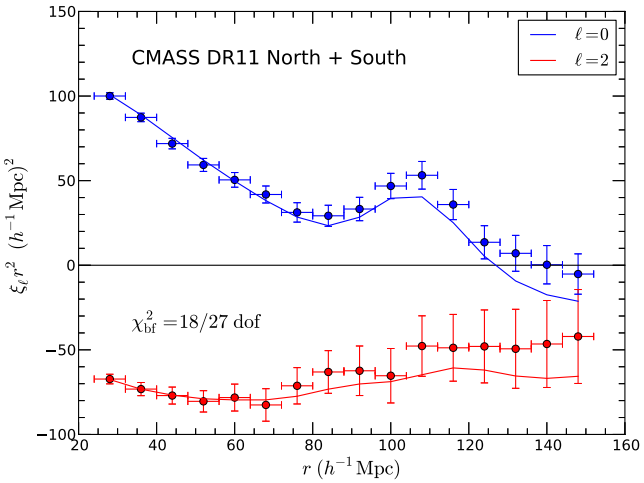

Figure 3. The measured monopole and quadrupole of DR11 sample as a function of redshift-space separation r. The solid lines show predictions of our best-fitting model with $\Omega_\mathrm{b}h^2 = 0.0222$, $\Omega_\mathrm{m}h^2 = 0.1408$, $n_\mathrm{s} = 0.962$, $b\sigma_8 = 1.29$, $f\sigma_8 = 0.437$, $\alpha_\perp = 1.017$, $\alpha_{||} = 1.001$ and $\sigma^2_\mathrm{FOG} = 12.6$.

4 THE COVARIANCES

To estimate the covariance matrix of our measurements, we use a suite of 600 PTHalo simulations. The simulations cover the same volume as the CMASS sample and are designed to produce a similar bias (for details of mock generation see Manera et al. 2013).

We compute the Legendre multipoles from each individual mock catalogue and estimate the covariance matrix as

$$C_{i,j}^{\ell,\ell'} = \frac{1}{N-1}\sum_k \left[\hat{\xi}_\ell^k(r_i) - \bar{\xi}_\ell(r_i)\right]\left[\hat{\xi}_{\ell'}^k(r_j) - \bar{\xi}_{\ell'}(r_j)\right], \tag{13}$$

where the sum is over individual mocks, and the average multipoles

$$\bar{\xi}_\ell(r_i) = \frac{1}{N}\sum_k \xi_\ell^k(r_i) \tag{14}$$

are also computed from the mocks. The unbiased estimator of the inverse covariance matrix is then given by

$$\mathbf{IC} = \frac{N-2-32}{N-1}\mathbf{C}^{-1} \tag{15}$$

where 32 is the number of bins used in the analysis (for details see Percival et al. 2013). Fig. 4 shows the reduced covariance matrix (diagonal elements normalized to one) of our multipoles. As expected, the measured multipoles in the neighbouring r-bins are strongly correlated. The correlation between measured monopole and quadrupole at the same scale is up to 15 per cent on smaller scales.

We will compute the likelihood of theoretical models as

$$\mathcal{L} \propto \exp\left(-\chi^2(\boldsymbol{p})/2\right), \tag{16}$$

where

$$\chi^2(\boldsymbol{p}) = \sum_{i,j,\ell,\ell'}\left(\hat{\xi}_\ell(r_i) - \xi_\ell^{\rm th}(r_i,\boldsymbol{p})\right)\widetilde{IC}_{i,j}^{\ell,\ell'}\left(\hat{\xi}_{\ell'}(r_j) - \xi_{\ell'}^{\rm th}(r_j,\boldsymbol{p})\right) \tag{17}$$

$\boldsymbol{p}$ are the set of parameters and ξ-th are the theoretical predictions for the multipoles. In equation (17), we additionally rescale the

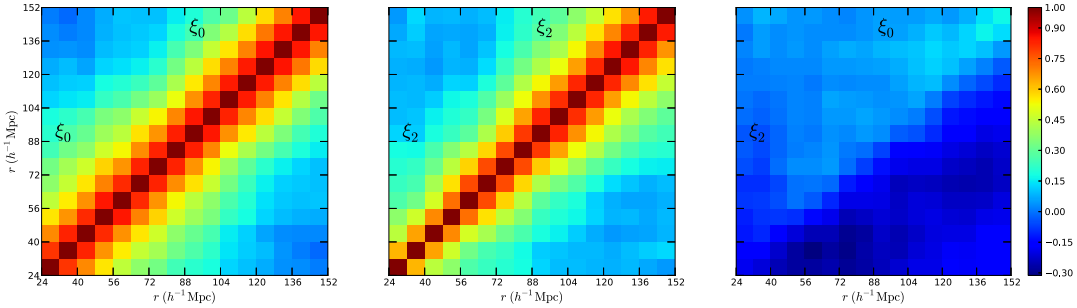

Figure 4. The reduced covariance matrix ($C_{i,j}/\sqrt{C_{i,i}C_{j,j}}$) of measured monopole and quadrupole in bins of $8\,h^{-1}$ Mpc in the range $24\,h^{-1} < r < 152\,h^{-1}$ Mpc estimated from 600 PTHalo mocks. The ξ_ℓ measurements in neighbouring bins are strongly correlated.

inverse covariance matrix

$$\widetilde{IC}_{i,j}^{\ell,\ell'} = IC_{i,j}^{\ell,\ell'} \times \frac{1 + B(n_\mathrm{b} - n_\mathrm{p})}{1 + A + B(n_\mathrm{p} - 1)}, \tag{18}$$

$$A = \frac{2}{(n_\mathrm{s} - n_\mathrm{b} - 1)(n_\mathrm{s} - n_\mathrm{b} - 4)}, \tag{19}$$

$$B = \frac{n_\mathrm{s} - n_\mathrm{b} - 2}{(n_\mathrm{s} - n_\mathrm{b} - 1)(n_\mathrm{s} - n_\mathrm{b} - 4)}, \tag{20}$$

where n_p is the length of vector $\boldsymbol{p}$. This accounts for the uncertainties in the determination of the inverse covariance matrix from the finite number of catalogues (for details see Percival et al. 2013). In our case, $n_\mathrm{s} = 600$, $n_\mathrm{b} = 32$ and $n_\mathrm{p} = 5$, which results in $A = 6.25 \times 10^{-6}$ and $B = 1.77 \times 10^{-3}$.[2] The multiplicative correction factor is then 1.04.

In approximating the likelihood by equations (16) and (17), we made two assumptions: that the errors on the monopole and quadrupole are drawn from a multivariate Gaussian distribution (equation 16) and that the dependence of inverse covariance matrix on free parameters is weaker than the dependence of the model $[\mathrm{d}IC_{i,j}^{\ell,\ell'}(\boldsymbol{p})/\mathrm{d}\boldsymbol{p} < \mathrm{d}\xi_\ell^\mathrm{th}(\boldsymbol{p})/\mathrm{d}\boldsymbol{p}$ in equation (17)].

Non-linear evolution will induce non-Gaussianity. To check the validity of the first assumption, we estimate a skewness of ξ_ℓ in bins of r from the 600 PTHalo mocks using

$$S_\ell(r_i) = \sqrt{600}\frac{\sum_k \left(\xi_\ell^k(r_i) - \bar{\xi}_\ell(r_i)\right)^3}{\left[\sum_k \left(\xi_\ell^k(r_i) - \bar{\xi}_\ell(r_i)\right)^2\right]^{3/2}}. \tag{21}$$

Fig. 5 shows a histogram of the resulting distribution of sample skewness and the prediction made assuming that the distribution of $\xi_\ell(r_i)$ is Gaussian. The observed distribution is consistent with the assumption of Gaussianity; therefore, we will ignore the contribution of possible non-Gaussian contributions to the likelihood of $\xi_\ell(r_i)$.

The validity of our second assumption is helped by the fact that the signal-to-noise ratio is high and the mock catalogues were tuned to reproduce the observed clustering of CMASS sample on average (see Manera et al. 2013 for details).

[2] We use $n_\mathrm{p} = 5$ here even though the total number of fitted parameters is 8, because the three 'shape' parameters are constrained almost exclusively by the Planck covariance matrix of equation (29) which is not derived from our suite of 600 PTHalo mocks and is assumed to be exact.

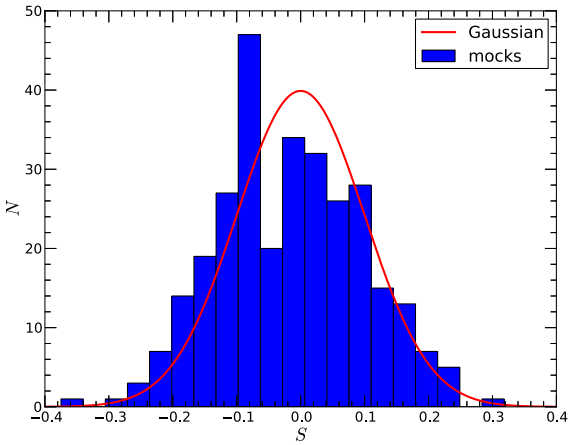

Figure 5. Histogram of the skewness of monopole and quadrupole measurements along with the expected distribution for a Gaussian variable. The empirical variance is compatible to the expectations from a Gaussian distribution.

5 THEORETICAL MODEL

5.1 Modelling multipoles

We use the 'streaming model' to compute our theoretical template correlation function. Within the streaming paradigm, the correlation function in redshift space is derived by taking a real space, isotropic correlation function $\xi^\mathrm{r}(r_{||}, r_\perp)$ and convolving it along the LOS with a probability distribution function of the infall velocity P of a galaxy pair at that separation.

$$1 + \xi^\mathrm{s}(s_{||}, s_\perp) = \int \left[1 + \xi^\mathrm{r}(r_{||}, r_\perp)\right] P(s_{||} - r_{||})\,\mathrm{d}r_{||}, \tag{22}$$

where $s_\parallel$ and $s_\perp$ are the components of a vector in the parallel and perpendicular to the LOS direction; $r_\parallel$ and $r_\perp$ are the analogous components in the real space. In the plane-parallel approximation, we adopt here $s_\perp = r_\perp$. The function P accounts for both quasi-linear infall motions and the random small-scale velocities ('Finger-of-God' effect; Jackson 1972).

Following Reid & White (2011), we assume

$$P(\Delta) = \frac{\exp\left(-\left[\Delta - \mu v_\mathrm{in}(r,\mu)\right]^2 / 2\left(\sigma_\mathrm{in}^2(r,\mu) + \sigma_\mathrm{FOG}^2\right)\right)}{\sqrt{2\pi\left(\sigma_\mathrm{in}^2(r,\mu) + \sigma_\mathrm{FOG}^2\right)}}, \tag{23}$$

and compute the $v_\mathrm{in}^2(r,\mu)$ and $\sigma_\mathrm{in}^2(r,\mu)$ values using the standard perturbation theory, while the correlation function in the configuration space – $\xi^\mathrm{r}(\boldsymbol{r})$ – is computed using Lagrangian perturbation

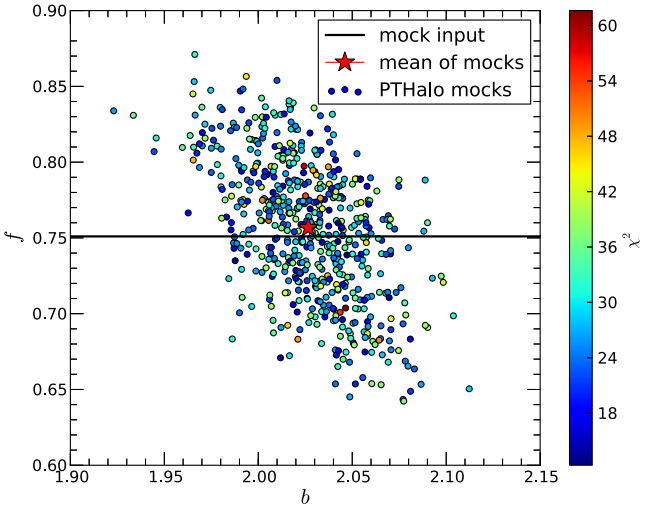

Figure 6. The value of growth rate recovered from 600 PTHalo mocks. The red star denotes the mock mean, while the solid black line denotes the input value.

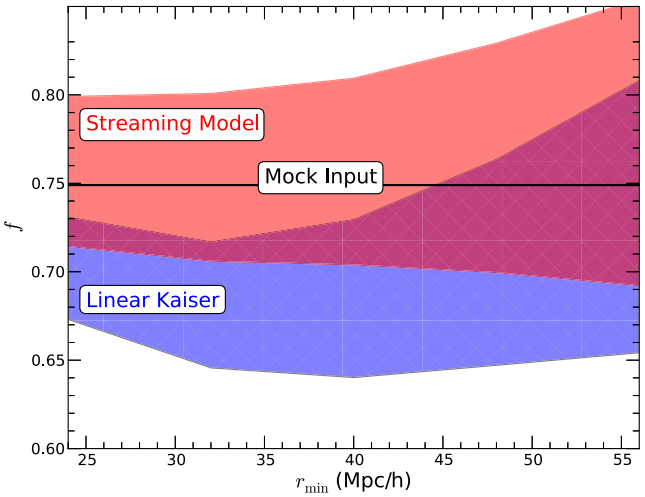

Figure 7. 1σ interval of f recovered by fitting the linear Kaiser model (blue hatched band) and our 'streaming model' (red band) to 600 PTHalo mocks as a function of minimum scale used in the analysis. The black solid line denotes f in the cosmology used to construct the mocks.

theory (see Reid & White 2011 for details). The parameter $\sigma^2_{\rm FOG}$ is an isotropic dispersion that accounts for motions of galaxies within their local environment that are approximately uncorrelated with the large-scale velocity field; this parameter is varied within a broad prior consistent with the expected contribution from satellite galaxies; see Reid et al. (2012) for further discussion.

Recently, Wang et al. (2014) extended the results of convolution Lagrangian perturbation (Carlson, Reid & White 2013) and combined them with the 'streaming model' to obtain accurate predictions for the two-dimensional correlation function. This improved model is accurate for a wider range of biases than the original model. For the CMASS sample, however, the original implementation of the model in Reid & White (2011) remains accurate enough and is used in this analysis (see also discussion following Fig. 6).

If the real geometry of the Universe differs from the fiducial cosmology used to compute the correlation function, this will result in the additional distortions via the AP effect. To account for this, we rescale the redshift-space correlation function in equation (23) as

$$\xi^{\rm obs}(s'_{\parallel}, s'_{\perp}) = \xi^{\rm s}(\alpha_{||} s_{||}, \alpha_{\perp} s_{\perp}), \tag{24}$$

where

$$\alpha_{\parallel} = \frac{H^{\rm fid}}{H}, \qquad \alpha_{\perp} = \frac{D_{\rm A}}{D_{\rm A}^{\rm fid}}, \tag{25}$$

and $H^{\rm fid}$ and $D_{\rm A}^{\rm fid}$ are the Hubble expansion rate and the angular distance in the fiducial cosmology.[3]

The model correlation function depends on the growth rate via $v_{\rm in}$ and $\sigma_{\rm in}$. The higher values of f result in higher amplitude of both multipoles. The dependence on the Hubble expansion rate and angular distance arise from the AP effect and are manifested as distortions of the multipole shapes.

Our model has been compared to N-body simulations and shown to fit the anisotropic clustering down to scales of $\sim 25\,h^{-1}$ Mpc with per cent level precision (Reid & White 2011; Reid et al. 2012). To check that the PTHalo mocks adequately describe the RSD signature in the range of scales used in the analysis, we fit our model to the mock measurements. For simplicity, we fix the shape of the linear power spectrum to the input value and use the input cosmology to compute radial and angular distances (this is equivalent to fixing $\alpha_{||} = \alpha_{\perp} = 1$) so that the only free parameters are f, b and $\sigma_{\rm FOG}$. Fig. 6 shows the distribution of maximum-likelihood (ML) values of b and f recovered from the mock catalogues. The systematic offset between the mean of the ML values for f and the input value of the mocks is of the order of 1 per cent, and the scatter in the ML values (after appropriate rescaling as in Percival et al. 2013) is comparable to the errors produced in Section 6. At least at the two-point level, this shows that the relevant systematic effects in the PTHalos mocks are much less than our measurement precision and can be safely ignored.

Fig. 7 shows the mean values and 1σ error bars recovered by fitting individual PTHalo mocks with the non-linear 'streaming model' as a function of minimal scale used in the analysis. The figure also shows the results if we use a linear theory model (Kaiser 1987) with no velocity dispersion nuisance parameter. We find that for the *BOSS* DR11 data, one would need to fit above 60 h^{-1} Mpc to get unbiased estimates of the growth rate with the linear model. The non-linear model resulted in unbiased fits even when scales down to $25\,h^{-1}$ Mpc were used.

The model predictions for $\xi_\ell(r)$ depend on eight parameters. These are parameters determining the shape of the linear correlation function $\boldsymbol{p}_{\rm sh} = (\Omega_{\rm m} h^2, \Omega_{\rm b} h^2, n_{\rm s})$, the bias of galaxies b, the linear growth rate f, two AP parameters $\alpha_{||}$ and $\alpha_{\perp}$, and FOG velocity dispersion, $\sigma^2_{\rm FOG}$. In linear theory, b and f are completely degenerate with σ_8, and observed clustering is only sensitive to their combination $b\sigma_8$ and $f\sigma_8$. Even though non-linear effects break this degeneracy, it is still present to high degree. To compute non-linear effects on the real-space correlation function as well as mean and variance of infall velocity, we need to specify a value of $\sigma_8(z = 0.57)$. In our analysis, we fix the value of $\sigma_8(z = 0.57) = 0.615$, which is the best-fitting value to *Planck* data within the ΛCDM-GR model. We checked that model predictions do not change significantly if we keep the values of $b\sigma_8$ and $f\sigma_8$ fixed and vary σ_8 within $\pm 3\sigma$ of the *Planck* constraints, and therefore, the recovered value of $f\sigma_8$ is not sensitive to the fiducial σ_8 used to compute non-linear effects. When combining our measurements with *Planck* data to constrain cosmological models, we do not fix a value of σ_8 and compute it for each model accordingly (see Section 7).

[3] These parameters were incorrectly defined in the text of Reid et al. (2012), but implemented correctly.

5.2 Modelling DE and gravity

The large-scale properties of the Universe after inflation depend on several variables. First, we have the relative abundances of the main energy-density constituents – radiation $\Omega_\gamma h^2$, baryons $\Omega_\mathrm{b} h^2$, dark matter $\Omega_\mathrm{dm} h^2$ and DE $\Omega_\mathrm{de} h^2$. We must also specify the parameters describing initial conditions at the end of inflation – the spectral index n_s and the amplitude of curvature perturbations Δ^2_R. Finally, the behaviour of DE can be fully described by its effective equation of state (EoS) $w(z)$ if the perturbations to DE fluid are negligible.

The energy density of radiation is determined with extremely high precision from the temperature of microwave background and is negligible at late times. In addition, the standard inflationary paradigm predicts the Universe to be spatially flat to a high degree, which means that the DE energy density can be expressed in terms of other components $\Omega_\mathrm{de} = 1 - \Omega_\mathrm{dm} - \Omega_\mathrm{b}$. The parameters Ω_dm, Ω_b and n_s are tightly constrained by CMB data in a way that is independent of late-time behaviour of DE and gravity. The CMB also provides a measurement of a distance to the last-scattering surface which depends on DE, but since it utilizes only one integrated measurement of distance, it results in highly degenerate constraints on $w(z)$ and Ω_m if used on its own.

The low-redshift measurements from anisotropic galaxy clustering are strongly complementary to CMB information. The quantities D_A and H depend on $\Omega_\mathrm{m} h^2 \equiv \Omega_\mathrm{dm} h^2 + \Omega_\mathrm{b} h^2$ and DE properties, breaking degeneracies of CMB data. The f in the $f\sigma_8$ measurement is sensitive to Ω_m. Relating σ_8 to Δ_R in a given model provides a strong additional test of both DE and gravity. The fluctuations in the galaxy field (σ_8 measured by RSD) are a result of initial fluctuations at recombination (Δ^2_R measured by CMB), and their relationship depends on the strength of gravity and expansion of the Universe from $z = 1000$ to the redshift of the galaxy sample. Even small offsets from GR and Λ are amplified and result in large offsets at low redshifts.

Independent probes of distance and expansion rate, such as measurements of luminosity distance from supernovae Type Ia (SNIa) or direct measurements of H, further enhance the cosmological constraints.

6 MEASUREMENTS

The measured monopole and quadrupole (see Section 3) along with the covariance matrix estimated from PTHalo mocks (see Section 4) are fitted with the predictions of the streaming model (see Section 5) to derive constraints on the geometry and the growth rate at an effective redshift of $\bar{z} = 0.57$.

The theoretical template for the multipoles depends on the parameters $\boldsymbol{p} = \left[b\sigma_8, f\sigma_8, \alpha_\parallel, \alpha_\perp, \Omega_\mathrm{m} h^2, \Omega_\mathrm{b} h^2, n_\mathrm{s}, \sigma^2_\mathrm{FOG}\right]$.

Constraints on the shape of the correlation function ($\boldsymbol{p}_\mathrm{sh}$) from CMB data are significantly tighter than similar constraints obtainable from galaxy clustering only, and these constraints are largely independent of either the behaviour of DE at low redshifts or the nature of gravity (i.e. the values of $\alpha_\parallel$, $\alpha_\perp$ and $f\sigma_8$ which are of main interest here). To exploit this fact, we multiply the likelihood in equation (16) by a *Planck* prior on this triplet

$$\mathcal{L}_\mathrm{full} = \mathcal{L}(\boldsymbol{p})\mathcal{L}_\mathrm{shape}(\boldsymbol{p}_\mathrm{sh}), \tag{26}$$

with

$$\chi^2(\boldsymbol{p}_\mathrm{sh}) = \Delta\boldsymbol{p}_\mathrm{sh}\mathbf{IC}_\mathrm{sh}\Delta\boldsymbol{p}^\mathrm{T}_\mathrm{sh} \tag{27}$$

and the mean values of $\boldsymbol{p}_\mathrm{sh}$ and the $\mathbf{IC}_\mathrm{sh}$ are given by *Planck* temperature anisotropy data (Planck Collaboration 2013). We use the shape prior derived from the combination of *Planck* temperature anisotropy data with the *WMAP* low-multipole polarization likelihood which is (Planck Collaboration 2013)

$$\begin{aligned} \Omega_\mathrm{c} h^2 &= 1.186 \times 10^{-1}, \\ \Omega_\mathrm{b} h^2 &= 2.218 \times 10^{-2}, \\ n_\mathrm{s} &= 9.615 \times 10^{-1}, \end{aligned} \tag{28}$$

$$\begin{array}{c} \\ \Omega_\mathrm{c} h^2 \\ \Omega_\mathrm{b} h^2 \\ n_\mathrm{s} \end{array} \begin{array}{c} \begin{array}{ccc} \Omega_\mathrm{c} h^2 & \Omega_\mathrm{b} h^2 & n_\mathrm{s} \end{array} \\ \begin{pmatrix} 5.44 \times 10^5 & 6.11 \times 10^5 & 1.33 \times 10^5 \\ 6.11 \times 10^5 & 2.04 \times 10^7 & -2.81 \times 10^5 \\ 1.33 \times 10^5 & -2.81 \times 10^5 & 6.75 \times 10^4 \end{pmatrix} \end{array}. \tag{29}$$

To explore this parameter space, we use the nested sampling method as implemented in the MULTINEST software package (Feroz, Hobson & Bridges 2009; Feroz et al. 2013). The free parameters of the model and their priors are listed in Table 1.

We have checked a posteriori that this range includes all the high-likelihood regions up to at least 5σ in all parameters except σ_FOG (see discussion in Section 6.1). The resulting constraints on main cosmological parameters are presented in Table 2.

To derive constraints on DE and MG parameters, we will be using the marginalized likelihood of parameters $D_\mathrm{V}/r_\mathrm{d}$, F and $f\sigma_8$, where $r_\mathrm{d}(\Omega_\mathrm{m} h^2, \Omega_\mathrm{b} h^2)$ is the sound horizon scale at the drag epoch. This marginalized likelihood can be approximated as a Gaussian with mean

$$\begin{aligned} D_\mathrm{V}/r_\mathrm{d} &= 13.85, \\ F &= 0.6725, \\ f\sigma_8 &= 0.4412 \end{aligned} \tag{30}$$

and covariance matrix

$$\begin{array}{c} \\ D_\mathrm{V}/r_\mathrm{d} \\ F \\ f\sigma_8 \end{array} \begin{array}{c} \begin{array}{ccc} D_\mathrm{V}/r_\mathrm{d} & F & f\sigma_8 \end{array} \\ \begin{pmatrix} 2.88 \times 10^{-2} & -9.67 \times 10^{-4} & -4.46 \times 10^{-4} \\ -9.67 \times 10^{-4} & 7.98 \times 10^{-4} & 9.70 \times 10^{-4} \\ -4.46 \times 10^{-4} & 9.70 \times 10^{-4} & 1.89 \times 10^{-3} \end{pmatrix} \end{array}. \tag{31}$$

Equations (30) and (31) use values of $r_\mathrm{d} = r_s(z_\mathrm{d})$ derived by numerically integrating the recombination equations and integrating the sound speed up to the drag epoch. These values are related to the results derived from commonly used fitting formula of Eisenstein & Hu (1998) adjusted by a factor of $r^\mathrm{EH}_\mathrm{d}/r_\mathrm{d} = 1.026$. This

Table 1. The priors on the model parameters.

Parameter	Min. value	Max. value
$b\sigma_8$	1.0	1.6
$f\sigma_8$	0.0	1.0
$\alpha_\parallel$	0.8	1.2
$\alpha_\perp$	0.8	1.2
σ_FOG	0.0	50.0
$\Omega_\mathrm{m} h^2$	0.08	0.14
$\Omega_\mathrm{b} h^2$	0.018	0.026
n_s	0.8	1.2

Table 2. Constraints on the model parameters.

Parameter	Central value	1σ error
$b\sigma_8$	1.29	0.03
$f\sigma_8$	0.441	0.043
$\alpha_\parallel$	1.006	0.033
$\alpha_\perp$	1.015	0.017

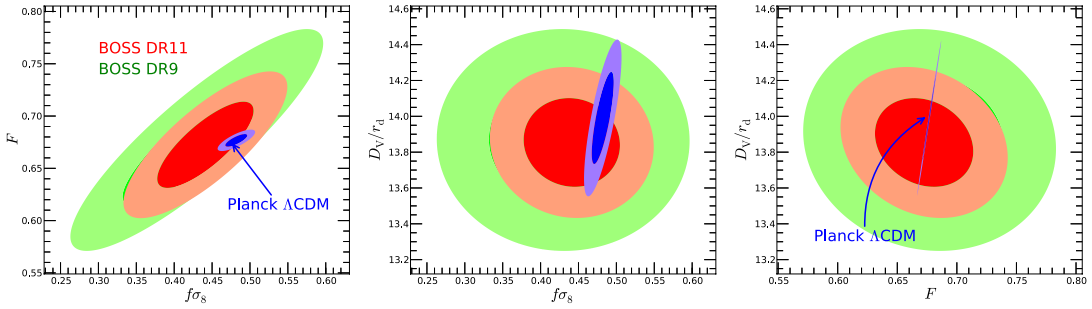

Figure 8. Posterior likelihood of parameters D_V/r_d, F and $f\sigma_8$ from *BOSS* DR11 (red contours) and *BOSS* DR9 (green contours) data, along with expectations from *Planck* data within standard ΛCDM-GR models (blue contours). All estimates are mutually consistent.

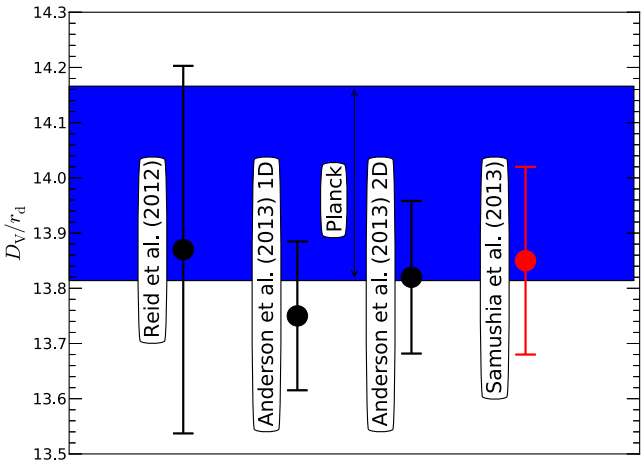

Figure 9. Various estimates of D_V/r_d from CMASS DR9 and DR11 data sets. The blue band corresponds to 1σ uncertainty in *Planck* prediction assuming ΛCDM. All measurements are mutually consistent.

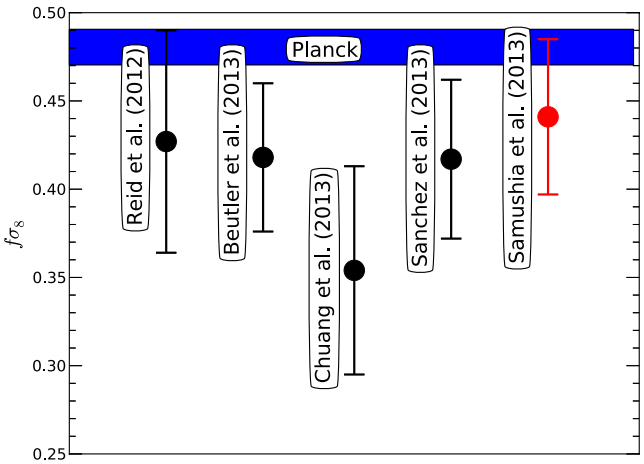

Figure 10. Various estimates of $f\sigma_8$ from CMASS DR9 and DR11. The blue band corresponds to 1σ uncertainty in *Planck* prediction assuming ΛCDM-GR. Clustering measurements are mutually consistent and are lower than the CMB prediction.

ratio is independent of cosmology for a wide range of conventional cosmological models (see e.g. Mehta et al. 2012).

Fig. 8 shows the constraints on main cosmological parameters compared to the expectations from the *Planck* data within standard ΛCDM-GR models along with DR9 results from Reid et al. (2012). The DR11 results are in a good agreement with the *Planck* predictions; the χ^2 difference between them is 1.6 for 3 degrees of freedom.

Equations (30) and (31) represent the main results of our work and will be used later to constrain models of DE and MG (see Section 7).

6.1 Comparison to other similar measurements

The companion papers, Anderson et al. (2013), Beutler et al. (2013), Sanchez et al. (2013b) and Chuang et al. (2013), use the same CMASS DR11 data to constrain the distance–redshift relation at $z = 0.57$.

Fig. 9 shows our measurement of distance along with the result from BAO-only fits and previous similar measurements and *Planck* predictions for spatially flat ΛCDM model.

In Fig. 9, the label 1D refers to the result derived by fitting the monopole of the correlation function only, while the label 2D refers to the result derived from the fit to the monopole and the quadrupole of the correlation function (see Anderson et al. 2013 for details). Anderson et al. (2013) differ from our analysis in two important aspects. They apply 'reconstruction' to the measured galaxy distribution to partially remove the non-linear smearing of the BAO feature, and marginalize over the broad-band shape of the correlation function, so that the estimate of the distance comes from the BAO peak feature alone.

Beutler et al. (2013) and Chuang et al. (2013) measured the distance–redshift relationship using the Legandre moments of power spectrum and correlation function, respectively. Beutler et al. (2013) perform their analysis in Fourier space. The Chuang et al. (2013) analysis is in configuration space but uses a different range of scales and theoretical model than our work. Despite differences in the applied methodology, the estimates are consistent within 1σ error bars.

The growth rate, $f\sigma_8$, has also been measured in the same redshift bin by Beutler et al. (2013, DR11), Reid et al. (2012, DR9), Chuang et al. (2013, DR11) and Sanchez et al. (2013b). The comparison of results is presented in Fig. 10. In the Sanchez et al. (2013b) analysis, $f\sigma_8$ is a derived parameter computed by combining CMASS data with *Planck* assuming ΛCDM model; their estimate is perfectly consistent with ours. The Reid et al. (2012) analysis is similar in the range of scales and theoretical modelling to the current paper, but performed on DR9 data set. All measurements are consistent with each other and are somewhat lower than the *Planck* ΛCDM-GR expectations.

6.1.1 Comparison with our DR9 measurements

The fitting methodology adopted in this paper is identical to that used in our DR9 analysis (Reid et al. 2012), but some of the priors have been updated. We adopt a prior on the linear matter power spectrum shape from *Planck* rather than *WMAP*7; *Planck* has substantially smaller errors, and so we expect the marginalization over the $P(k)$ to contribute negligibly to our error budget in DR11. We also adopted a slightly more conservative top-hat prior on $\sigma^2_{\rm FOG}$, by increasing the allowed range from 0–40 to 0–50 Mpc^2, as the large-scale clustering data alone cannot well constrain this dispersion term; we have checked that this change of prior range does not affect our best-fitting parameter values significantly.

The effective area of DR11 is a factor of 2.5 larger than DR9; in the limit of negligible boundary effects, we would expect the covariance matrix on $D_{\rm V}/r_{\rm d}$, F and $f\sigma_8$ to be reduced by the same factor. A direct comparison indicates agreement at the ∼15 per cent level on the diagonals, with DR11 errors slightly larger than expected and with different off-diagonal structure. When projected on to $f\sigma_8$ (at fixed $D_{\rm V}/r_{\rm d}$ and F), which is the relevant case for the modified gravity constraints we present, our error in DR9 was 0.033 and is 0.028 in DR11, while we would have expected 0.021 from the effective volumes. This situation arises because, as we showed in table 2 of Reid et al. (2012), the prior on $\sigma^2_{\rm FOG}$ reduces the uncertainty on $f\sigma_8$ in the fixed geometry case substantially. The statistical errors have shrunk significantly in DR11, but we did not assume better prior knowledge on $\sigma^2_{\rm FOG}$.

A measurement of $\sigma^2_{\rm FOG}$ from small-scale clustering is in progress (Reid et al., in preparation); if this parameter were perfectly known, the $f\sigma_8$ error would be reduced to 0.017 when the geometric and power spectrum parameters are held fixed.

In DR11, we obtain higher values for $D_{\rm V}/r_{\rm s}$ and $f\sigma_8$, which brings us slightly closer to the values predicted by *Planck*. The χ^2 offset between DR11 and DR9 results is just 0.3 per 3 degrees of freedom.

6.2 Constraints from monopole and quadrupole separately

To determine the separate contribution of monopole and quadrupole, we perform the same fit to each individually. The monopole and quadrupole measurements on their own are unable to break the degeneracy between $b\sigma_8$ and $f\sigma_8$, and can only constrain combinations of the two. Fig. 11 shows the constrains in $b\sigma_8$–$f\sigma_8$ derived from the two multipoles. The solid lines show the expected degeneracy directions based on linear theory predictions.

The quadrupole best constrains $A_2 = (4/3bf + 4/7f^2)\sigma_8^2$, as expected from the linear theory. The amplitude constraints from monopole are collinear to the combination $A_0 = (b^2 + 2/3bf + 1/5f^2)\sigma_8^2$, also as expected from the linear theory.

The AP parameters $\alpha_{||}$ and $\alpha_\perp$ show a qualitatively similar picture. Individual multipoles can only constrain certain combinations of parameters. Fig. 12 presents constraints in the $\alpha_{||}$–$\alpha_\perp$ plane from the monopole and quadrupole separately. The solid lines show the expected degeneracy directions based on the linear theory predictions.

The principal component of the monopole constraint coincides with $\alpha_{\rm V} = \sqrt[3]{\alpha_\perp^2 \alpha_{||}}$ as expected from the linear theory. The principal component of the quadrupole constraint is slightly tilted from the $\alpha_\epsilon \equiv \alpha_\perp/\alpha_{||} = {\rm const}$ direction; $\alpha_{\rm V} = 1.011 \pm 0.013$ from the monopole and $\alpha_\epsilon = 0.988 \pm 0.091$ from the quadrupole.

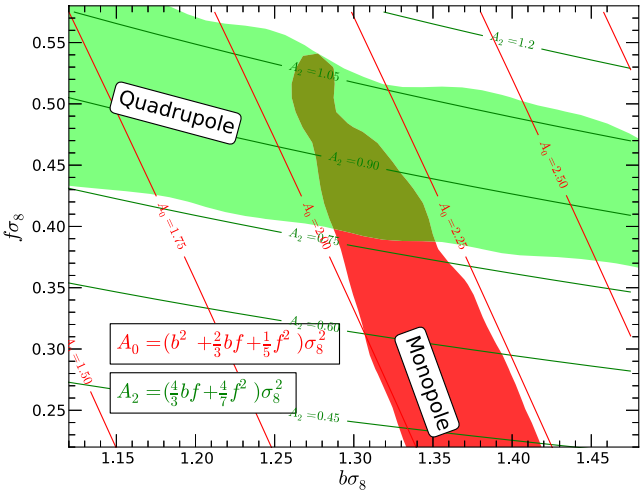

Figure 11. Constraints on $b\sigma_8$ and $f\sigma_8$ from monopole and quadrupole separately. The solid lines show expected directions of the principal components based on predictions of the linear theory.

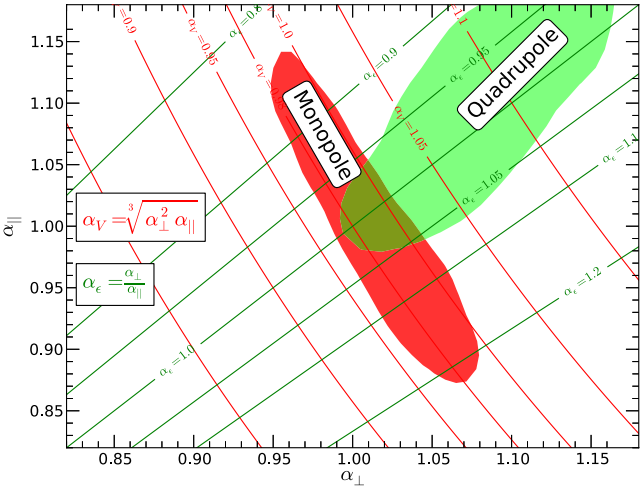

Figure 12. Constraints on $\alpha_{||}$ and $\alpha_\perp$ from monopole and quadrupole separately. The solid lines show expected directions of the principal components based on predictions of the linear theory.

6.3 Separate fits to growth and AP

We next fit the monopole and quadrupole for the growth factor and AP parameters separately. First, we assume that the background expansion follows the predictions of spatially flat ΛCDM but allows the growth rate to be a free parameter. In this case, the parameters $\alpha_\parallel$ and $\alpha_\perp$ can be computed from $\Omega_{\rm m}$ and H_0. For this model, where the background expansion is assumed to be following the ΛCDM predictions, we find $f\sigma_8 = 0.447 \pm 0.028$ and $b\sigma_8 = 1.26 \pm 0.02$. The constraint on growth improves to 6 per cent (from 10 per cent) and is perfectly consistent with the result of our more general fit.

Next, we assume that the growth rate follows the predictions of ΛCDM-GR, but let the expansion rate and the distance–redshift relation vary. In this case, $f\sigma_8$ is computed from $\Omega_{\rm m}$ but the $\alpha_\parallel$ and $\alpha_\perp$ are free parameters. For this fit, we obtain $\alpha_\parallel = 0.992 \pm 0.023$ and $\alpha_\perp = 1.021 \pm 0.013$. Constraints on $\alpha_\parallel$ move to a lower value and tighten to 2 per cent (from 3 per cent), while constraints on $\alpha_\perp$ move to a higher value and tighten to 1 per cent (from 2 per cent).

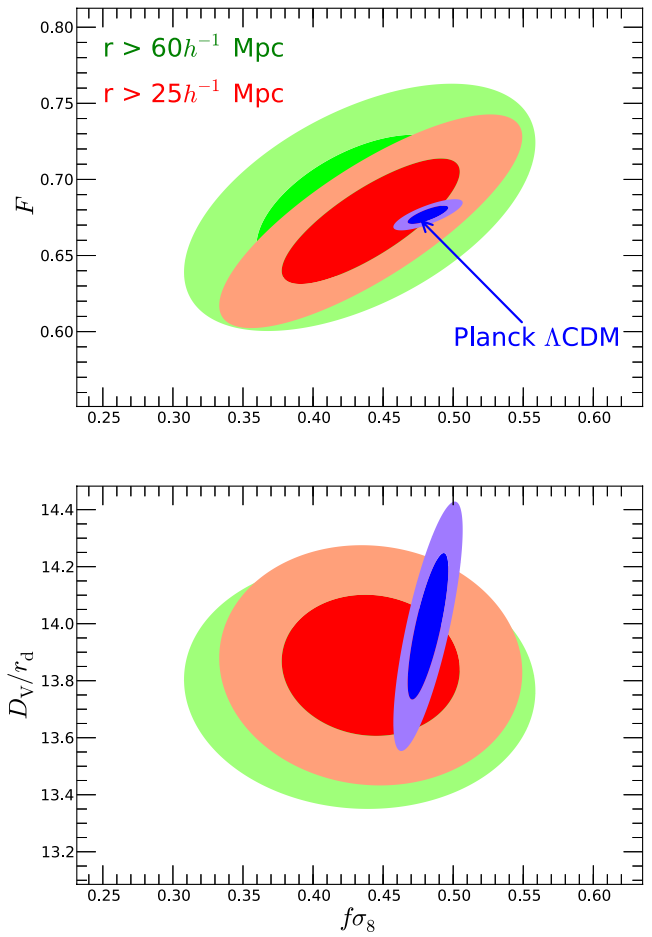

Figure 13. Constraints on $f\sigma_8$, F and D_V/r_d from large scales only (green contours) and from all scales (red contours), along with predictions of ΛCDM-GR normalized by the *Planck* results. All estimates are mutually consistent.

6.4 Contribution from small scales

Moments of the correlation function are measured with the best signal-to-noise ratio at small scales. The model that we use has been tested against numerical simulations with agreement at the per cent level down to $r \simeq 25\,h^{-1}$ Mpc. To determine explicitly the contribution of small scales on our fits, we redo the fit to the monopole and quadrupole keeping only scales above $r = 60\,h^{-1}$ Mpc. The results of this fit and the comparison to the main results are shown in Fig. 13.

The inclusion of scales between $30\ h^{-1} < r < 60\,h^{-1}$ Mpc improves our constraints by approximately a factor of 2. For the main parameters of interest, we find $b\sigma_8 = 1.28 \pm 0.07$, $f\sigma_8 = 0.433 \pm 0.050$, $D_V/r_d = 13.78 \pm 0.17$ and $F = 0.682 \pm 0.033$. The biggest improvement is in the variables that are determined from the amplitudes of the multipoles such as $b\sigma_8$, $f\sigma_8$ and F. Improvement in D_V/r_d is more modest, because most of the information about this quantity is produced by the BAO peak in the monopole at $r \simeq 100\,h^{-1}$ Mpc.

Small-scale clustering pushes $f\sigma_8$ and D_V/r_d to higher values and F to lower values. The two estimates, however, are highly consistent, the χ^2 offset between the two being $\chi^2 = 0.29$ for 3 degrees of freedom. Both sets of measurements are consistent with *Planck* data. The χ^2 difference between large-scale-only measurements and *Planck* inferred values is 1.8 for 3 degrees of freedom, while the difference between large-scale-only measurements and the ones using all scales above $25\,h^{-1}$ Mpc is 0.3 for 3 degrees of freedom.

Table 3. Constraints on basic parameters of ΛCDM-GR.

	ΛCDM-GR		
Parameter	*ePlanck*	BOSS + *ePlanck*	BOSS + *ePlanck* + BAO
$100\Omega_b\,h^2$	2.21 ± 0.03	2.21 ± 0.02	2.22 ± 0.02
Ω_Λ	0.685 ± 0.017	0.692 ± 0.011	0.696 ± 0.009
n_s	0.960 ± 0.007	0.961 ± 0.006	0.962 ± 0.005
$\sigma_8(0)$	0.829 ± 0.012	0.823 ± 0.011	0.821 ± 0.011
100τ	8.91 ± 1.30	8.91 ± 1.24	9.02 ± 1.23
H_0	67.3 ± 1.2	67.8 ± 0.84	68.1 ± 0.7

7 COSMOLOGICAL IMPLICATIONS

In following subsections, we constrain parameters of standard ΛCDM-GR model by combining our measurements with the CMB and previous, independent BAO measurements. We also examine possible deviations from the standard model by considering phenomenological modifications to both Λ and GR parts.

As a CMB data set, we adopt the recent measurements of CMB temperature fluctuations by the *Planck* satellite (Planck Collaboration 2013) supplemented by low-ℓ measurements of CMB polarization from the *WMAP* misssion (Bennett et al. 2013) and the high-ℓ measurements from the Atacama Cosmology Telescope (Das et al. 2013) and the South Pole Telescope (Reichart, Shaw & Zahn 2012). For the rest of the paper, we will refer to this combination of CMB data as *ePlanck*.[4] For our BAO data compilation we use measurements from Beutler et al. (2011, $z = 0.106$), Anderson et al. (2013, $z = 0.32$)[5] and Blake et al. (2011b, $z = 0.60$).

To sample cosmological parameter space, we use the Monte Carlo Markov Chain (MCMC) technique implemented by the COSMOMC package (Lewis & Bridle 2002).

7.1 ΛCDM-GR

In a spatially flat ΛCDM-GR model, the expansion history of the Universe and the growth of perturbations can be fully described by six parameters. We choose these to be $\boldsymbol{p}_{\Lambda\mathrm{CDM}} = \left[\Omega_\Lambda, \Omega_b\,h^2, n_s, \sigma_8(0), \tau, H_0\right]$. The mean values and 1σ confidence levels are listed in Table 3.

By combining *BOSS* DR11 results with *Planck* data, we are able to achieve a 1.6 per cent constraint on Ω_Λ, a 1.3 per cent constraint on $\sigma_8(0)$ and a 1.2 per cent constraint on H_0. After including BAO data set, the constraints improve to 1.3 per cent on Ω_Λ and a 1.0 per cent constraint on H_0, while relative constraint on $\sigma_8(z = 0)$ does not change. The constraints on Ω_b and n_s are dominated by the information from the *ePlanck* data set.

[4] When computing the CMB likelihood, we make the same assumptions as Planck Collaboration (2013). For example, we assume a minimum neutrino mass of $\sum m_\nu = 0.06$ eV. This affects the time of matter-radiation equality and angular-diameter distance to last scattering, as well as early integrated Sachs–Wolfe effect and the lensing potential.

[5] We only use a measurement of BAO from the lower redshift (LOWZ) sample since the measurement from the CMASS sample is highly correlated with our own estimate of D_V/r_d.

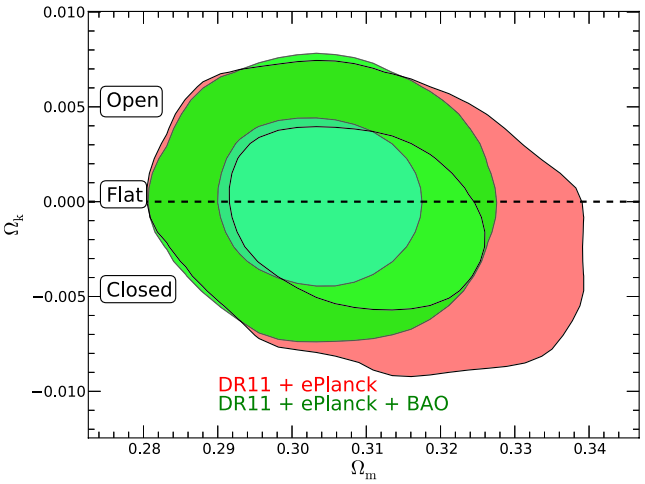

Figure 14. Constraints on spatial curvature and non-relativistic matter density from the combination of *BOSS* DR11 data with CMB and BAO data sets. The contours correspond to 1σ and 2σ confidence levels in posterior likelihood.

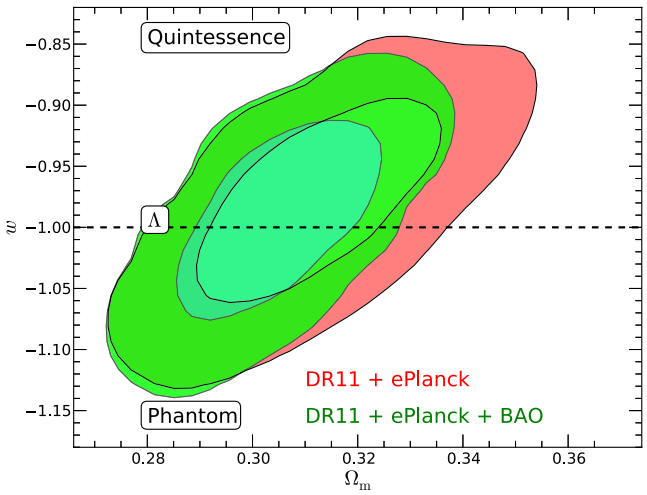

Figure 15. Constraints on w and non-relativistic matter density from the combination of *BOSS* DR11 data with CMB and BAO data sets. The contours correspond to 1σ and 2σ confidence levels in posterior.

7.2 Spatial curvature

We now relax the assumption that the spatial curvature is zero and allow the Ω_k parameter to vary along with $\boldsymbol{p}_{\Lambda\mathrm{CDM}}$. The posterior confidence regions on curvature and non-relativistic matter density are shown in Fig. 14.

We find $1 + \Omega_k = 0.999 \pm 0.003$ (a 0.3 per cent constraint) when combining *BOSS* DR11 with *ePlanck* and $1 + \Omega_k = 1.000 \pm 0.003$ (a 0.3 per cent constraint) when adding the BAO compilation. In both cases, the results are perfectly consistent with a spatially flat Universe.

7.3 Time dependence of dark energy

Alternative models of DE predict a time-dependent EoS $w(z)$. For a wide range of DE models that do not exhibit sudden transitions or large amount of DE at early times, for example models based on cosmological scalar fields, this time-dependence can be adequately parametrized by two parameters

$$w(z) = w_0 + w_a \frac{z}{1+z} \tag{32}$$

(Chevallier & Polarski 2001; Linder 2003). (For DE models that do not belong to this family see e.g. Wetterich 2004; Doran & Robbers 2006.) This reduces to our standard model for $w_0 = -1$ and $w_a = 0$.

We first set w_a to zero and check if there is an evidence for w to differ from -1 on average. The confidence level contours on w and non-relativistic matter density are shown in Fig. 15.

This analysis yields $w = -0.983 \pm 0.075$ (a 8 per cent constraint) when *BOSS* DR11 is combined with *ePlanck* data and $w = -0.993 \pm 0.056$ (a 6 per cent constraint) when the BAO compilation is added. In both cases, the results are perfectly consistent with a cosmological constant ($w = -1$). Our constraints on w differ significantly from the DR9 results presented in Samushia et al. (2013), where we detected up to 2σ preference for $w > -1$. This change is mainly due to two differences. We now use *ePlanck* as our CMB data set, which predicts a higher value for the non-relativistic matter density. Also, our new measurements, although consistent with DR9 results, have moved in the direction that makes them more consistent with the CMB results (see Fig. 8).

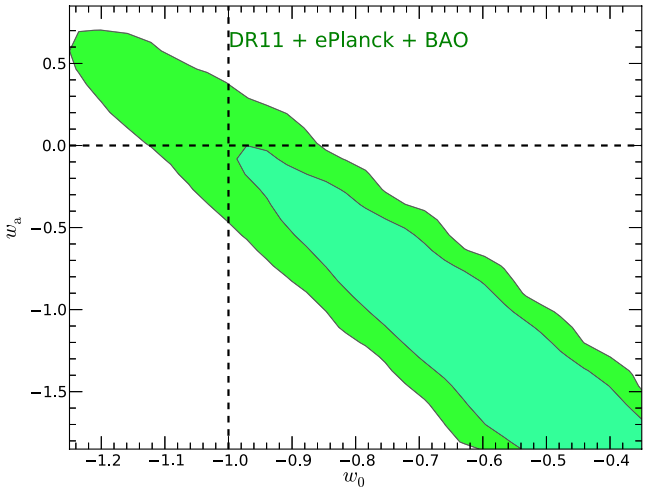

Figure 16. Constraints on w and w_a from the combination of *BOSS* DR11 data with CMB and BAO data sets. The contours correspond to 1σ and 2σ confidence levels in posterior likelihood. The ΛCDM prediction is consistent at the 1.5σ level.

Finally, we consider a model in which the spatial curvature is a free parameter and both w_0 and w_a are allowed to vary. The constraints on this model are shown in Fig. 16. The DR11 data alone, even after combining with *ePlanck*, is not able to break all the degeneracies of this large parameter space. When DR11 and *ePlanck* are combined with the BAO, we see a preference for larger values of w_0 and smaller values of w_a. The ΛCDM value of $w_0 = -1$ and $w_a = 0$, however, is still within the 2σ confidence level.

7.4 Deviations from GR

MG predict scale dependence of bias and growth rate even in the linear regime and the effect of small-scale screening mechanisms is difficult to model. This makes devising a completely self-consistent test of MG models a non-trivial task. A number of proposals for parametrizing families of MG models have been discussed recently (see e.g. Battye & Pearson 2012; Bloomfield et al. 2012; Baker, Ferreira & Skordis 2013; Mueller, Bean & Watson 2013). These

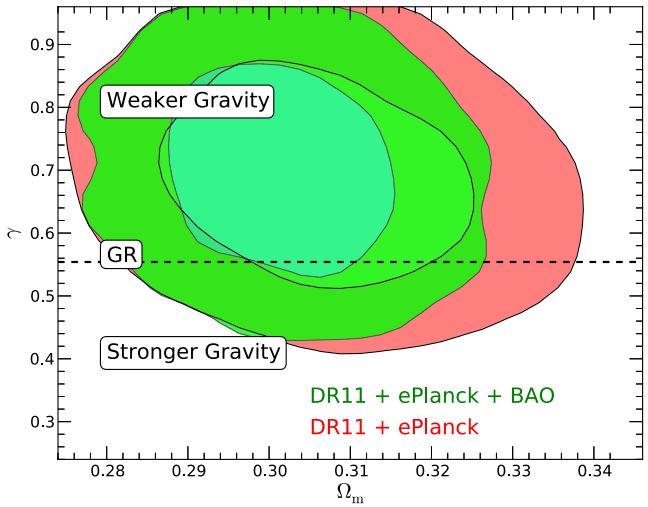

Figure 17. Constraints on γ-index and non-relativistic matter density from the combination of *BOSS* DR11 data with CMB, SNIa, BAO and H_0 data sets. The contours correspond to 1σ and 2σ confidence levels in posterior likelihood. The best fit is consistent with GR at 1σ.

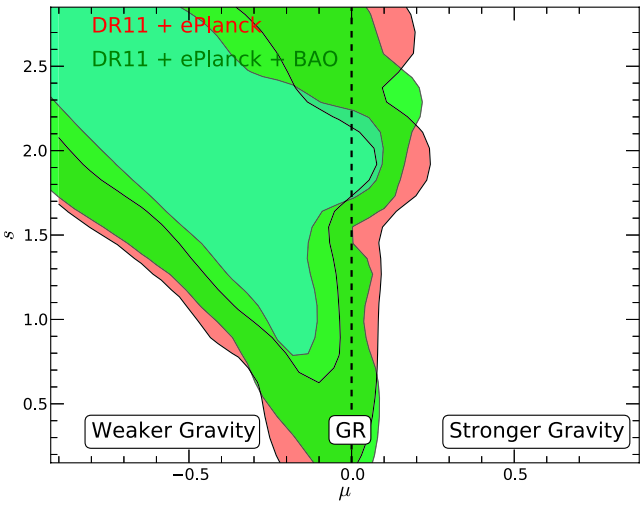

Figure 18. Constraints on μ and s from the combination of *BOSS* DR11 data with CMB and BAO data sets. The contours correspond to 1σ and 2σ confidence levels in posterior likelihood.

parametrizations, however, are difficult to correctly implement in practice for a few reasons. First, they rely on the linear theory and are not expected to work below scales of $\sim 25\,h^{-1}$ Mpc. Secondly, they require a large number of free parameters and such a large parameter space cannot be effectively constrained by current data. For these reasons, we follow the approach of Samushia et al. (2013) and apply several few-parameter consistency tests to our measurements.

We parametrize the growth rate as a function of Ω_m using

$$f = \left[\frac{\Omega_m(z)}{E(z)}\right]^{\gamma} \tag{33}$$

(Linder & Cahn 2008). This approach does not provide a fully self-consistent test of MG models, as MG models predict a more complex change in observables compared to GR. This parametrization is, however, easy to implement and provides a simple consistency test. In GR, we expect the γ-index to be equal to 0.554. Measuring a significantly higher value would indicate a preference for a force weaker than GR gravity and vice versa. In our fits, we apply a hard prior of $\gamma < 1.0$.

When constraining deviations from GR, we fix DE to be a cosmological constant. We also ignore the CMB power spectrum on large scales ($\ell < 50$) to ensure that CMB data are used only to constrain the background evolution. The parametrizations that we use are not physically motivated and are simply meant to describe effective gravity at low redshifts rather than provide a full model that works accurately at all redshifts up to last-scattering surface.

Constraints on γ and Ω_m are shown in Fig. 17. When combining *BOSS* DR11 with *ePlanck* data, we recover $\gamma = 0.691 \pm 0.111$ (a 16 per cent measurement). With the BAO data set, we recover $\gamma = 0.699 \pm 0.110$ (a 16 per cent measurement). The values are within 1.2σ confidence of GR values but favour a weaker gravity.

Next, we parametrize the linear equation of growth following the approach of Pogosian et al. (2010) as

$$\ddot{\delta} + \left(2 + \dot{H}\right)\dot{\delta} = \frac{3}{2}\Omega_m(z) G\delta\left(1 + \mu a^s\right), \tag{34}$$

where δ is a matter overdensity, the overdot denotes a derivative with respect to $\ln a$, G is the gravitational constant, and μ and s are parameters describing deviations from GR. The GR limit is recovered when $\mu = 0$, where negative values of μ correspond to weaker than GR gravity and vice versa. The s parameter dictates how rapidly the modifications are set, with larger values of s corresponding to the modifications that appear at later times. Since large values of s correspond to models in which gravity is indistinguishable from GR until some low redshift when the modification suddenly becomes significant, they are basically unconstrained. We place a flat prior of $0 < s < 3$ to avoid this problem. The confidence level contours of μ and s are shown in Fig. 18.

The GR predictions are within 2σ in posterior likelihood. Similar to γ-parametrization, the data again provide a mild preference for a weaker than GR gravity. This result is consistent with the DR9-based results reported in Samushia et al. (2013).

8 CONCLUSIONS

We have used the anisotropic clustering of galaxies in the *BOSS* DR11 data set to simultaneously constrain the growth rate, the redshift–distance relationship and the expansion rate at the redshift of $z = 0.57$. Overall, our measurements are in good agreement with the results of the *Planck* satellite propagated to low redshifts assuming ΛCDM-GR.

By combining our measurements of $f\sigma_8$, D_V and F with the CMB data we were able to derive tight constraints on basic cosmological parameters and parameters describing deviations from the ΛCDM-GR model. We were able to constrain the curvature of Universe with 0.3 per cent precision, the DE EoS parameter w with 8 per cent precision and the γ-index for growth with 16 per cent precision.

When we vary the background expansion within ΛCDM predictions of the *Planck* data, we measure the growth rate (parametrized by γ) to be weaker but consistent within 1.2σ of GR predictions. This preference for lower values of growth rate has also been observed in other similar low-redshift measurements (see e.g. Macaulay, Wehus & Eriksen 2013 for discussion). Our measurement of $f\sigma_8$ follows this trend but is closer to the GR predictions compared to the DR9 results of Reid et al. (2012) and the DR11 measurement of Beutler et al. (2013).

Similar measurements from a lower redshift (LOWZ) sample of *BOSS* galaxies will provide a complementary measurement of the

growth rate in the DE-dominated redshift range of $0.2 < z < 0.43$, which will significantly strengthen the constraining power over possible GR modifications and can potentially increase the significance of the 'low growth rate' signal.

ACKNOWLEDGEMENTS

LS gratefully acknowledges support by the European Research Council. BAR gratefully acknowledges support provided by NASA through Hubble Fellowship grant 51280 awarded by the Space Telescope Science Institute, which is operated by the Association of Universities for Research in Astronomy, Inc., for NASA, under contract NAS 5-26555. Funding for SDSS-III has been provided by the Alfred P. Sloan Foundation, the Participating Institutions, the National Science Foundation and the US Department of Energy Office of Science. The SDSS-III website is http://www.sdss3.org/.

SDSS-III is managed by the Astrophysical Research Consortium for the Participating Institutions of the SDSS-III Collaboration including the University of Arizona, the Brazilian Participation Group, Brookhaven National Laboratory, University of Cambridge, Carnegie Mellon University, University of Florida, the French Participation Group, the German Participation Group, Harvard University, the Instituto de Astrofisica de Canarias, the Michigan State/Notre Dame/JINA Participation Group, Johns Hopkins University, Lawrence Berkeley National Laboratory, Max Planck Institute for Astrophysics, Max Planck Institute for Extraterrestrial Physics, New Mexico State University, New York University, Ohio State University, Pennsylvania State University, University of Portsmouth, Princeton University, the Spanish Participation Group, University of Tokyo, University of Utah, Vanderbilt University, University of Virginia, University of Washington and Yale University.

We acknowledge the use of MCMC data from Planck Legacy Archive (http://www.sciops.esa.int/index.php?project=planck&page=Planck_Legacy_Archive).

Numerical computations were done on the Sciama High Performance Compute cluster which is supported by the ICG, SEPNet and the University of Portsmouth.

REFERENCES

Albrecht A. et al., 2009, preprint (arXiv:0901.0721)
Alcock C., Paczynski B., 1979, Nature, 281, 358
Anderson L. et al., 2012, MNRAS, 427, 3435
Anderson L. et al., 2013, MNRAS, preprint (arXiv:1312.4877)
Baker T., Ferreira P. G., Skordis C., 2013, Phys. Rev. D, 87, 024015
Ballinger W. E., Peacock J. A., Heavens A. F., 1996, MNRAS, 282, 877
Bassett B. A., Hlozek R., 2010, in Ruiz-Lapuente P., ed., Dark Energy: Observational and Theoretical Approaches. Cambridge Univ. Press, Cambridge, p. 246
Battye R. A., Pearson J. A., 2012, J. Cosmol. Astropart. Phys., 7, 019
Bennett C. L. et al., 2013, ApJS, 208, 20
Beutler F. et al., 2011, MNRAS, 416, 3017
Beutler F. et al., 2012, MNRAS, 423, 3430
Beutler F. et al., 2013, MNRAS, 429, 3604
Bianchi D., Guzzo L., Branchini E., Majerotto E., de la Torre S., Marulli F., Moscardini L., Angulo R. E., 2012, MNRAS, 427, 2420
Blake C., Brough S., Colless M., Contreras C., 2011a, MNRAS, 415, 2876
Blake C., Kazin E. A., Beutler F., Davis T. M., 2011b, MNRAS, 418, 1707
Blake C., Brough S., Colless M., Contreras C., 2012, MNRAS, 425, 405
Bloomfield J. K., Flanagan E. E., Park M., Watson S., 2012, J. Cosmol. Astropart. Phys., 08, 010
Bolton A. et al., 2012, AJ, 144, 144
Carlson J., Reid B. A., White M., 2013, MNRAS, 429, 1674
Chevallier M., Polarski D., 2001, Int. J. Mod. Phys. D, 10, 213
Chuang C.-H., Wang Y., 2013, MNRAS, 431, 2634
Chuang C.-H. et al., 2012, MNRAS, 433, 3559
Chuang C.-H. et al., 2013, MNRAS, preprint (arXiv:1312.4889)
Crocce M., Scoccimarro R., Bernardeau F., 2012, MNRAS, 427, 2537
Das S. et al., 2013, preprint (arXiv:1301.1037)
Dawson K. et al., 2013, AJ, 145, 10
de la Torre S., Guzzo G., 2012, MNRAS, 427, 327
de la Torre S. et al., 2013, A&A, 557, 54
Doran M., Robbers G., 2006, J. Cosmol. Astropart. Phys., 06, 026
Eisenstein D. J., Hu W., 1998, ApJ, 496, 605
Eisenstein D. J., Seo H.-J., White M., 2007, ApJ, 664, 660
Eisenstein D. J. et al., 2011, AJ, 142, 72
Elia A., Kulkarni S., Porciani C., Pietroni M., Matarrese S., 2011, MNRAS, 116, 1703
Feldman H. A., Kaiser N., Peacock J. A., 1994, ApJ, 426, 23
Feroz F., Hobson M. P., Bridges M., 2009, MNRAS, 398, 1601
Feroz M., Hobson M. P., Cameron E., Pettitt A. N., 2013, preprint (arXiv:1306.2144)
Fukugita M., Ichikawa T., Gunn J. E., Doi M., Shimasaku K., Schneider D. P., 1996, AJ, 111, 1748
Gil-Marin H., Wagner C., Verde L., Porcini C., Jimenez R., 2012, J. Cosmol. Astropart. Phys., 11, 029
Gunn J. E. et al., 2006, AJ, 116, 3040
Gunn J. E. et al., 2013, AJ, 126, 32
Guzzo L. et al., 2008, Nature, 451, 541
Hamilton A. J. S., 1998, in Hamilton D., ed., Astrophysics Space Science Library, Vol. 231, The Evolving Universe. Kluwer, Dordrecht, p. 185
Jackson J. C., 1972, MNRAS, 156, 1
Kaiser N., 1987, MNRAS, 227, 1
Kazin E. A., Sanchez A. G., Blanton M. R., 2012, MNRAS, 419, 3223
Landy S. D., Szalay A. S., 1993, ApJ, 412, 64
Lewis A., Bridle S., 2001, Phys. Rev. D, 66, 103511
Linder E. V., 2003, Phys. Rev. Lett., 90, 091
Linder E. V., Cahn R. N., 2008, Astropart. Phys., 28, 481
Macaulay E., Wehus I. K., Eirksen H. K., 2013, Phys. Rev. Lett., 111, 161301
Manera M. et al., 2013, MNRAS, 428, 1036
Marulli F., Bianchi D., Branchini E., Guzzo L., Moscardini L., Angulo R. E., 2012, MNRAS, 426, 2566
Mehta K. T., Cuesta A. J., Xiaoying X., Eisenstein D. J., Padmanabhan N., 2012, MNRAS, 427, 2168
Meiksin A., White M., Peacock J. A., 1999, Mem. R. Astron. Soc., 304, 851
Mueller E.-M., Bean R., Watson S., 2013, Phys. Rev. D, 87, 083504
Okamura T., Taruya A., Matsubara T., 2011, J. Cosmol. Astropart. Phys., 8, 12
Padmanabhan N., Xu X., Eisenstein D. J., Scalzo R., Cuesta A. J., Mehta K. T., Kazin E., 2012, MNRAS, 427, 2132
Percival W. J. et al., 2014, MNRAS, in press
Planck Collaboration, 2013, preprint (arXiv:1303.5076)
Pogosian L., Silvestri A., Koyama K., Zhao G.-B., 2010, Phys. Rev. D, 81, 104023
Rapetti D., Blake C., Allen S. W., Mantz A., Parkinson D., Beutler F., 2013, MNRAS, 432, 973
Reichart C. L., Shaw L., Zahn O., 2012, ApJ, 755, 23
Reid B. A., White M., 2011, MNRAS, 417, 1913
Reid B. A. et al., 2012, MNRAS, 426, 2719
Ross A. J. et al., 2012, MNRAS, 424, 564
Ross A. J. et al., 2014, MNRAS, 437, 1109
Samushia L. et al., 2011, MNRAS, 410, 1993
Samushia L., Percival W. J., Raccanelli A., 2012, MNRAS, 420, 2102
Samushia L. et al., 2013, MNRAS, 429, 1514
Sanchez A. et al., 2013a, MNRAS, 433, 1202
Sanchez A. et al., 2013b, MNRAS, preprint (arXiv:1312.4854)
Simpson F. et al., 2013, MNRAS, 429, 2249
Smee S. A. et al., 2013, AJ, 126, 32
Strateva I. et al., 2001, AJ, 122, 1861

Taruya A., Nishimichi T., Saito S., 2010, Phys. Rev. D, 82, 063522
Taruya A., Saito S., Nishimichi T., 2011, Phys. Rev. D, 83, 103527
Vlah Z., Seljak U., McDonald P., Okamura T., Baldauf T., 2012, J. Cosmol. Astropart. Phys., 11, 009
Wang L., Reid B. A., White M., 2013, MNRAS, 437, 588
Weinberg D. H., Mortonson M. J., Eisenstein D. J., Hirata C., Reiss A. G., Eduardo R., 2013, Phys. Rep., 530, 87
Wetterich C., 2004, Phys. Lett. B, 594, 17
Zhao G.-B., Li H., Linder E. V., Koyama K., Bacon D. J., Zhang X., 2012, Phys. Rev. D, 85, 123546

APPENDIX A: CMB SHAPE PRIOR

Fig. A1 displays the posterior likelihood of $p_{\rm sh}$ obtainable from DR11 data alone.

The likelihood surface does not close even within $\pm 10\sigma$ of the CMB constraints. Previous studies either fix the shape parameters to their CMB best-fitting values (e.g. Samushia et al. 2012), let $\Omega_{\rm m} h^2$ vary and fix the rest (e.g. Blake et al. 2011a), or marginalize over them by taking a prior centred around CMB best-fitting values (e.g. Chuang et al. 2012).

We adopt a different approach and apply the CMB shape prior to our galaxy clustering likelihood. Since later we will combine our results with *Planck* data to obtain constraints on DE and MG parameters, one may be led to an erroneous impression that the CMB data are being double counted. We demonstrate below that this is not the case.

Let $\mathcal{L}^{\rm C}(a, b)$ be a CMB likelihood, where a are shape parameters and b are other parameters that may be related to DE and gravity parameters of interest $[b(w, \gamma, \dots)]$. Let $\mathcal{L}^{\rm G}(a, c)$ be galaxy likelihood, where c are DE and gravity dependent $[c(w, \gamma, \dots)]$. For simplicity, assume a, b and c to be scalars and that all likelihoods are multivariate Gaussian.

In our approach, we take a CMB shape prior

$$\int \mathcal{L}^{\rm C}(a, b)\, {\rm d}b \tag{A1}$$

apply it to galaxy data

$$\int \mathcal{L}^{\rm C}(a, b) L^{\rm G}(a, c)\, {\rm d}b\, {\rm d}a \tag{A2}$$

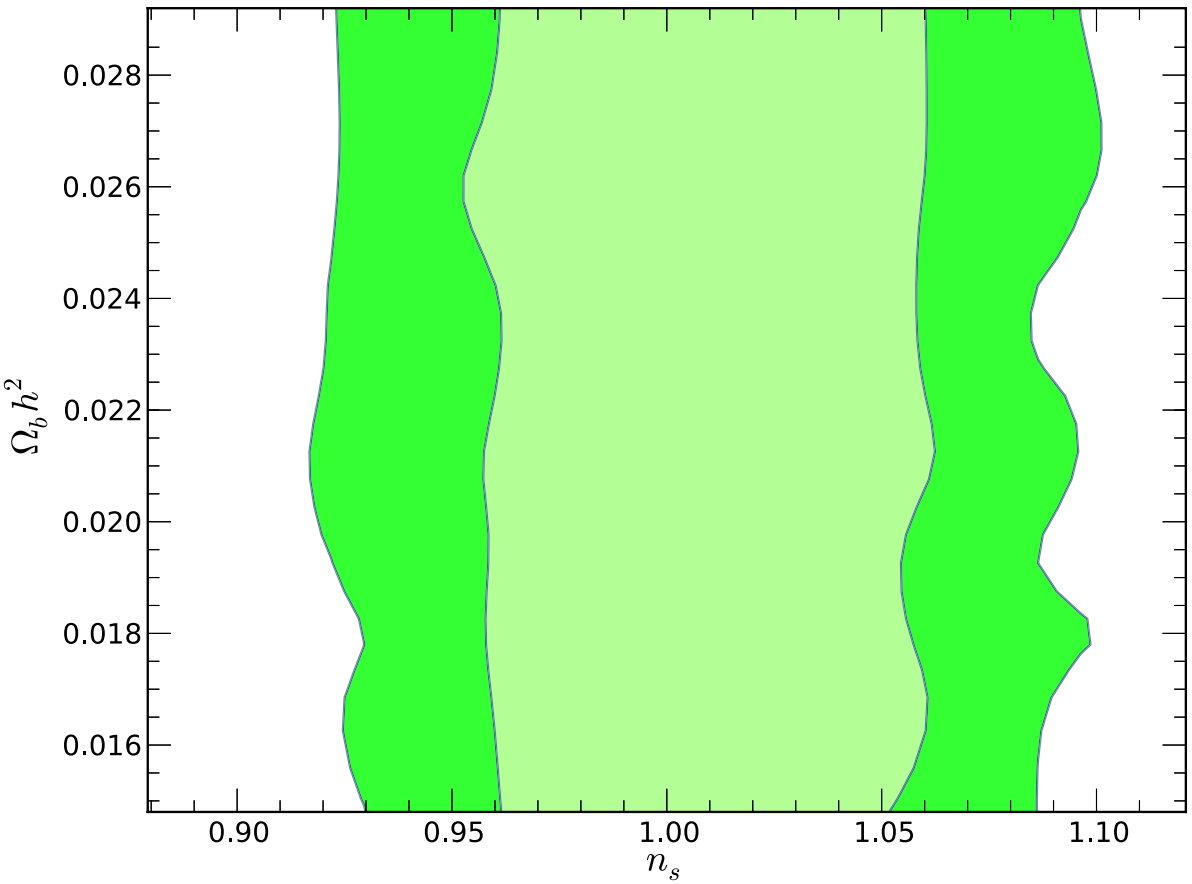

Figure A1. Posterior likelihood in $p_{\rm sh}$ from *BOSS* DR11 data only. The $\Omega_{\rm b}$ remains unconstrained in a 10σ range around the CMB measurement.

and then combine it with full CMB likelihood

$$\mathcal{L}_1(b'(x)c(x)) = \int \mathcal{L}^{\rm C}(a,b)\mathcal{L}^{\rm G}(a,c)\mathcal{L}^{\rm C}(a',b')\,{\rm d}b\,{\rm d}a\,{\rm d}a', \tag{A3}$$

where $x = (w, \gamma, \dots)$.

Let us compare this expression to that produced by directly combining the two likelihoods

$$\mathcal{L}_2(b(x)c(x)) = \int \mathcal{L}^{\rm C}(a,b)\mathcal{L}^{\rm G}(a,c)\,{\rm d}a. \tag{A4}$$

$\mathcal{L}_1(b,c)$ and $\mathcal{L}_2(b,c)$ are also Gaussian with

$$\sigma_{1b}^2 = \sigma_{Cb}^2 \tag{A5}$$

$$\sigma_{1c}^2 = \frac{\sigma_{Ca}^2 + \sigma_{Ga}^2(1-r_{Gac})}{\sigma_{Ca}^2+\sigma_{Ga}^2}\sigma_{Gc}^2 \tag{A6}$$

$$\rho_{1bc} = 0 \tag{A7}$$

$$\sigma_{2b}^2 = \frac{\left(\sigma_{Ca}^2(1-r_{Cab})+\sigma_{Ga}^2\right)\left(\sigma_{Ca}^2(1-r_{Cab})+\sigma_{Ga}^2(1-r_{Gac})\right)}{\sigma_{Ca}^4(1-r_{Cab})+\sigma_{Ca}^2\sigma_{Ga}^2\left(2-r_{Gac}^2-r_{Cab}^2-3r_{Cab}^2r_{Gac}^2\right)+\sigma_{Ga}^4(1-r_{Gab})}\sigma_{Cb}^2$$

$$\sigma_{2c}^2 = \frac{\left(\sigma_{Ca}^2+\sigma_{Ga}^2(1-r_{Gac})\right)\left(\sigma_{Ca}^2(1-r_{Cab})+\sigma_{Ga}^2(1-r_{Gac})\right)}{\sigma_{Ca}^4(1-r_{Cab})+\sigma_{Ca}^2\sigma_{Ga}^2\left(2-r_{Gac}^2-r_{Cab}^2-3r_{Cab}^2r_{Gac}^2\right)+\sigma_{Ga}^4(1-r_{Gab})}\sigma_{Gc}^2$$

$$\rho_{2bc} = \frac{r_{Gac}r_{Cab}\sigma_{Ca}\sigma_{Ga}\sigma_{Cb}\sigma_{Gc}\left(\sigma_{Ca}^2(1-r_{Cab})+\sigma_{Ga}^2(1-r_{Gac})\right)}{\sigma_{Ca}^4(1-r_{Cab})+\sigma_{Ca}^2\sigma_{Ga}^2\left(2-r_{Gac}^2-r_{Cab}^2-3r_{Cab}^2r_{Gac}^2\right)+\sigma_{Ga}^4(1-r_{Gab})}.$$

$\mathcal{L}_2$ always encloses $\mathcal{L}_1$. To first order in σ_{Ca}/σ_{Ga}

$$\sigma_{1b}^2 = \sigma_{Cb}^2 \tag{A8}$$

$$\sigma_{1c}^2 = (1-r_{\rm Gac})\sigma_{Gc}^2 \tag{A9}$$

$$\rho_{1bc} = 0 \tag{A10}$$

$$\sigma_{1b}^2 = \sigma_{Cb}^2 \tag{A11}$$

$$\sigma_{1c}^2 = (1-r_{\rm Gac})\sigma_{Gc}^2 \tag{A12}$$

$$\rho_{1bc} = r_{Gac}r_{Cab}\sigma_{Cb}\sigma_{Gc}\frac{\sigma_{Ca}}{\sigma_{Cb}}. \tag{A13}$$

This demonstrates that direct combination of galaxy clustering and CMB data always produces stronger constraints on derived parameters, and therefore the galaxy clustering measurements obtained by assuming a CMB prior on the shape can be combined with the CMB data without double counting the information.

This paper has been typeset from a TEX/LATEX file prepared by the author.